Karlsruher Institut für Technologie
Institut für Baustatik

A Finite element formulation for piezoelectric shell structures considering geometrical and material nonlinearities

K. Schulz, S. Klinkel, W. Wagner

Mitteilung 3(2010)

BAUSTATIK

Karlsruher Institut für Technologie
Institut für Baustatik

A Finite element formulation for piezoelectric shell structures considering geometrical and material nonlinearities

K. Schulz, S. Klinkel, W. Wagner

Mitteilung 3(2010)

Prof. Dr.–Ing. W. Wagner
Institut für Baustatik
Karlsruher Institut für Technologie
Kaiserstr. 12
76131 Karlsruhe

Telefon: (0721) 608–2280
Telefax: (0721) 608–6015
E–mail: info@ibs.kit.edu
Internet: http://www.ibs.kit.edu

A Finite element formulation for piezoelectric shell structures considering geometrical and material nonlinearities

K. Schulz[1], S. Klinkel[2] and W. Wagner[1]

[1]Karlsruhe Institute of Technology(KIT), Institute for Structural Analysis, Kaiserstr.12, 76131 Karlsruhe, Germany

[2]Statik u. Dynamik d. Tragwerke, Technische Universität Kaiserslautern, Paul-Ehrlich-Str. 14, D-67663 Kaiserslautern, Germany

Abstract In this paper we present a nonlinear finite element formulation for piezoelectric shell structures. Based on a mixed multi field variational formulation, an electro-mechanical coupled shell element is developed considering geometrically and materially nonlinear behavior of ferroelectric ceramics. The mixed formulation includes the independent fields of displacements, electric potential, strains, electric field, stresses, and dielectric displacements. Besides the mechanical degrees of freedom, the shell counts only one electrical degree of freedom. This is the difference of the electric potential in thickness direction of the shell. Incorporating nonlinear kinematic assumptions, structures with large deformations and stability problems can be analyzed. According to a Reissner-Mindlin theory, the shell element accounts for constant transversal shear strains. The formulation incorporates a three-dimensional transversal isotropic material law, thus the kinematic in thickness direction of the shell is considered. The normal zero stress condition and the normal zero dielectric displacement condition of shells are enforced by the independent resultant stress and resultant dielectric displacement fields. Accounting for material nonlinearities, the ferroelectric hysteresis phenomena are considered using the Preisach model. As a special aspect, the formulation includes temperature-dependent effects and thus the change of the piezoelectric material parameters due to the temperature. This enables the element to describe temperature dependent hysteresis curves.

1 Introduction

Piezoelectric material plays an important role for sensor and actuator devices. In the course of optimization of systems, shell structures have become more and more interesting. In recent years, several piezoelectric shell formulations based on the finite element method have been introduced. One can distinguish between solid shell elements, see e.g. References [1, 2, 3], and classical formulations, which model the shell by a reference surface, see e.g. References [4, 5, 6, 7, 8, 9, 10, 11]. Some of these element formulations are restricted to shallow shell structures, [5, 6, 9, 11], where the initial shell curvature is assumed to be small. In order to consider laminated structures, the above mentioned formulations include a more or less sophisticated laminate theory. References [5, 10, 12, 13, 14] point out that geometrically nonlinear characteristics can significantly influence the performance of piezoelectric systems, especially for the sensor usage. A geometrically nonlinear theory that incorporates large rotations is presented in References [1, 5, 6, 12]. A common assumption in piezoelectric models is that the electric field is constant through the thickness. This is not correct for bending dominated problems. According to Reference [15], a quadratic approach for the electric potential through the thickness is necessary to fulfill the electric charge conservation law. Shell formulations incorporating a quadratic thickness potential can be found in References [16, 8, 7]. Mixed

shell formulations including independent fields for the electric potential, the electric field, the dielectric displacement as well as the mechanical fields of the displacement, the strain, and the stress can be found in [19].
Accounting for nonlinear material behavior, the polarization state has to be analyzed. Due to high electric fields, ferroelectric switching processes take place and the material properties change. To consider the resultant ferroelectric hysteresis phenomena, one can refer to microscopic models, see References [20, 21], and macroscopic models, see e.g. References [22, 23, 24, 25, 26, 27, 28]. Microscopic analysis looks at single crystals and models the switching process via an energy criterion. A macroscopic approach using a switching criterion based on thermodynamic energy function is presented in [22, 23, 24, 25, 26, 27]. Macroscopic phenomenological hysteresis models can be found in Reference [28]. A well known phenomenological model is the Preisach model, see Reference [47]. Several piezo-mechanical coupled formulations have used the Preisach model to display piezoelectric material behavior, see References [30, 31, 32]. A shell element that accounts for material nonlinearities is [33]; it is based on a phenomenological switching function. In order to consider the nonlinear material behavior in a classical shell formulation, the strain and the electric field in thickness direction have to be comprised. A classical mechanical shell element incorporating three dimensional constitutive equations is e.g. proposed by Reference [34]. The influence of the temperature on piezoelectric material behavior has been studied experimentally in References [36, 37, 38, 39]. [39] shows that the ferroelectric hysteresis curves become smaller with increasing temperature. A micropolar model to consider the temperature-dependent relation between the electric field and the polarization is introduced by [40]. Here, the influence of mechanical stress is neglected and there is no remark on the strain behavior. A simple one-dimensional phenomenological model considering the strain is presented in Reference [41]. The authors assume a volume part of paraelectric phase for every hysteresis. [35] presents a piezoelectric plate element considering the deformation of a linear temperature gradient through the thickness, and gives the results depending on the piezoelectric material parameters for different temperature levels. Thus, temperature can influence the performance of piezoelectric shell structures due to a change of the temperature dependent material parameters. The essentiell aspects of the piezoelectric shell formulation presented in this paper are the following:

(i) The bilinear, four-node shell element is based on a six field variational functional. Besides the six mechanical degrees of freedom, three displacements and three rotations, the only electrical degree of freedom is the difference of the electric potential in thickness direction;

(ii) The element includes nonlinear kinematic assumptions, thus a geometric nonlinear analysis becomes feasible;

(iii) The formulation incorporates three dimensional transversal isotropic constitutive equations. In the shell formulation a linear approach for both the strain and the electric field in thickness direction is considered;

(iv) Using the Preisach model, the material nonlinear ferroelectric hysteresis effects are incorporated. Here the change of the saturation parameters of the polarization and the strain due to temperature is phenomenologically included, thus temperature-dependent hysteresis curves can be determined.

2 Kinematics

We model the shell by a reference surface Ω with the boundary Γ. Every point of Ω is part of the Euklidean space $\mathcal{B}$. In order to display the geometry of the structure in $\mathcal{B}$, we denote a convected coordinate system of the body $\boldsymbol{\xi}^i$ and an origin O with the global cartesian coordinate system $\mathbf{e}_i$. The initial thickness of the shell in the reference configuration is given as h, thus we define the arbitrary reference surface by the thickness coordinate $\xi^3 = 0$ with $h_- \leq \xi^3 \leq h_+$. $\mathbf{X}(\xi^1, \xi^2)$ and $\mathbf{x}(\xi^1, \xi^2)$ denote the position vectors of the shell surface Ω by means of the convective coordinates in the reference and the current configuration respectively. The covariant tangent vectors for the reference and the current configuration, $\mathbf{A}_i$ and $\mathbf{a}_i$, are given as

$$\mathbf{A}_i = \frac{\partial \mathbf{X}}{\partial \xi^i}, \qquad \mathbf{a}_i = \frac{\partial \mathbf{x}}{\partial \xi^i}, \qquad i = 1, 2, 3 \quad . \tag{1}$$

The contravariant basis $\mathbf{A}^i$ is defined by the orthogonality $\delta_i^j = \mathbf{A}_i \cdot \mathbf{A}^j$. The director vector $\mathbf{D}(\xi^1, \xi^2)$ with $|\mathbf{D}(\xi^1, \xi^2)| = 1$ is given perpendicular to Ω. It holds $\mathbf{D} = \mathbf{A}_3$. We obtain the corresponding inextensible director vector $\mathbf{d}$ of the current configuration with the rotation tensor $\mathbf{R}$ by the orthogonal transformation $\mathbf{d} = \mathbf{R}\mathbf{D}$. In the following, we refer to the notation that Latin indices range from 1 to 3 and Greek indices range from 1 to 2, whereas we use the summation convention for repeated indices. Commas denote a partial differentiation with respect to the coordinates ξ^α. A displacement $\mathbf{u}$ can be determined by the difference of the current and the initial position vectors $\mathbf{u} = \mathbf{x} - \mathbf{X}$. Including a Reissner-Mindlin kinematic, we consider transverse shear strain, thus it holds $\mathbf{d} \cdot \mathbf{x}_{,\alpha} \neq 0$. For the geometric in-plane and thickness strains we assume

$$\begin{aligned} E_{\alpha\beta} &= \varepsilon_{\alpha\beta} + \xi^3 \, \kappa_{\alpha\beta} \\ 2E_{\alpha 3} &= \gamma_\alpha \\ E_{33} &= 0 \quad . \end{aligned} \tag{2}$$

We write the membrane strains $\varepsilon_{\alpha\beta}$, the curvatures $\kappa_{\alpha\beta}$, and the shear strains γ_α of the shell, see Reference [42], as

$$\begin{aligned} \varepsilon_{\alpha\beta} &= \frac{1}{2}(\mathbf{x}_{,\alpha} \cdot \mathbf{x}_{,\beta} - \mathbf{X}_{,\alpha} \cdot \mathbf{X}_{,\beta}) \\ \kappa_{\alpha\beta} &= \frac{1}{2}(\mathbf{x}_{,\alpha} \cdot \mathbf{d}_{,\beta} + \mathbf{x}_{,\beta} \cdot \mathbf{d}_{,\alpha} - \mathbf{X}_{,\alpha} \cdot \mathbf{D}_{,\beta} - \mathbf{X}_{,\beta} \cdot \mathbf{D}_{,\alpha}) \\ \gamma_\alpha &= \mathbf{x}_{,\alpha} \cdot \mathbf{d} - \mathbf{X}_{,\alpha} \cdot \mathbf{D} \quad . \end{aligned} \tag{3}$$

The electric field $\vec{\mathbf{E}} = \begin{bmatrix} \vec{E}_1 & \vec{E}_2 & \vec{E}_3 \end{bmatrix}^T$ is given as the gradient field of the electric potential φ. Due to the shell geometry, we assume that the piezoelectric material is poled in thickness direction and the electrodes are arranged at the lower and upper surface. Therefore, we only consider the difference of the electric potential in thickness direction of the shell $\Delta\varphi$ and write the geometric electric field $\vec{\mathbf{E}}_g = \begin{bmatrix} \vec{E}_1 & \vec{E}_2 & 0 \end{bmatrix}^T$ as

$$\vec{\mathbf{E}}_g = -\frac{\partial \Delta\varphi}{\partial \xi^i} \mathbf{A}^i \quad . \tag{4}$$

We summarize the strains and the electric field of the shell in a generalized geometric strain vector $\boldsymbol{\varepsilon}_g(\mathbf{v})$

$$\boldsymbol{\varepsilon}_g(\mathbf{v}) = [\varepsilon_{11}, \varepsilon_{22}, 2\varepsilon_{12}, \kappa_{11}, \kappa_{22}, 2\kappa_{12}, \gamma_1, \gamma_2, \vec{E}_1, \vec{E}_2]^T \quad . \tag{5}$$

Herein, it holds $\mathbf{v} = [\mathbf{u}, \boldsymbol{\omega}, \Delta\varphi]^T$, with the displacements $\mathbf{u}$, the rotational parameters $\boldsymbol{\omega}$, and the difference of the electric potential $\Delta\varphi$.

The components of the Green-Lagrangean strains $\mathbf{E} = \frac{1}{2}(\mathbf{C} - \mathbf{1})$ as function of the right Cauchy-Green tensor $\mathbf{C} = \mathbf{F}^T\mathbf{F}$ with the deformation gradient $\mathbf{F}$ and the electric field are arranged in the column matrix $\boldsymbol{\varepsilon} = \begin{bmatrix} E_{11} & E_{22} & E_{33} & 2E_{12} & 2E_{13} & 2E_{23} & \vec{E}_1 & \vec{E}_2 & \vec{E}_3 \end{bmatrix}^T$. The independent shell vector under consideration of the thickness components of the strain ε_{33} and the electric field $\vec{E}_3$ is given as

$$\bar{\boldsymbol{\varepsilon}} = \begin{bmatrix} \tilde{\varepsilon}_{11} & \tilde{\varepsilon}_{22} & 2\tilde{\varepsilon}_{12} & \tilde{\kappa}_{11} & \tilde{\kappa}_{22} & 2\tilde{\kappa}_{12} & \tilde{\gamma}_1 & \tilde{\gamma}_2 & \tilde{\vec{E}}_1 & \tilde{\vec{E}}_2 & \tilde{\varepsilon}^0_{33} & \tilde{\varepsilon}^1_{33} & \tilde{\vec{E}}^0_3 & \tilde{\vec{E}}^1_3 \end{bmatrix}^T .$$

Here, $\tilde{\varepsilon}^0_{33}$ and $\tilde{\varepsilon}^1_{33}$ describe the constant and linear components of the thickness strain, $\tilde{\vec{E}}^0_3$ and $\tilde{\vec{E}}^1_3$ describe the constant and linear part of the electric field. We define the relation between the Green-Lagrangean strains and the independent shell strains by

$$\boldsymbol{\varepsilon} = \boldsymbol{A}\bar{\boldsymbol{\varepsilon}} \quad , \tag{6}$$

with

$$\boldsymbol{A} = \begin{bmatrix} 1 & 0 & 0 & \xi^3 & 0 & 0 & 0 & 0 & 0 & 0 & 0 & 0 & 0 & 0 \\ 0 & 1 & 0 & 0 & \xi^3 & 0 & 0 & 0 & 0 & 0 & 0 & 0 & 0 & 0 \\ 0 & 0 & 0 & 0 & 0 & 0 & 0 & 0 & 0 & 0 & 1 & \xi^3 & 0 & 0 \\ 0 & 0 & 1 & 0 & 0 & \xi^3 & 0 & 0 & 0 & 0 & 0 & 0 & 0 & 0 \\ 0 & 0 & 0 & 0 & 0 & 0 & 1 & 0 & 0 & 0 & 0 & 0 & 0 & 0 \\ 0 & 0 & 0 & 0 & 0 & 0 & 0 & 1 & 0 & 0 & 0 & 0 & 0 & 0 \\ 0 & 0 & 0 & 0 & 0 & 0 & 0 & 0 & 1 & 0 & 0 & 0 & 0 & 0 \\ 0 & 0 & 0 & 0 & 0 & 0 & 0 & 0 & 0 & 1 & 0 & 0 & 0 & 0 \\ 0 & 0 & 0 & 0 & 0 & 0 & 0 & 0 & 0 & 0 & 0 & 0 & 1 & \xi^3 \end{bmatrix} . \tag{7}$$

3 Constitutive equations

We introduce linear constitutive equations with the Green-Lagrangean strain $\mathbf{E}$, the Lagrangean electric field $\vec{\mathbf{E}}$, the second Piola-Kirchhoff stresses $\mathbf{S}$, and the dielectric displacements $\vec{\mathbf{D}}$. Focusing on our material model, here we neglect thermal stresses and pyroelectric effects. For a detailed description of thermal effects and its impact on the piezoelectric response, as e.g. thermal buckling, see References [6, 43]. We write the simplified constitutive equation as

$$\underbrace{\begin{bmatrix} \mathbf{S} \\ -\vec{\mathbf{D}} \end{bmatrix}}_{\boldsymbol{\sigma}} = \underbrace{\begin{bmatrix} \mathbb{C} & -\mathbb{e}^T \\ -\mathbb{e} & -\boldsymbol{\epsilon} \end{bmatrix}}_{\bar{\mathbb{C}}} \underbrace{\begin{bmatrix} \mathbf{E} \\ \vec{\mathbf{E}} \end{bmatrix}}_{\boldsymbol{\varepsilon}} \quad . \tag{8}$$

The strains and the electric fields are summarized in the vector $\boldsymbol{\varepsilon}$. The dependent variables of the stresses and the dielectric displacements are summarized in $\boldsymbol{\sigma}$ with $\boldsymbol{\sigma} = \begin{bmatrix} S_{11} & S_{22} & S_{33} & S_{12} & S_{13} & S_{23} \end{bmatrix}$ The three dimensional elasticity matrix $\mathbb{C}$, the permittivity matrix $\boldsymbol{\epsilon}$, and the piezoelectric coupling modulus $\mathbb{e}$ are arranged in $\bar{\mathbb{C}}$. In $\mathbb{C}$, we assume transversal isotropic material behavior with isotropy in the 23-plane, which can be specified with five independent parameters,

see [44]. The polarization in thickness direction of the structure leads to a piezoelectric modulus $\mathfrak{e}$ with three independent coefficients and a permittivity matrix $\boldsymbol{\epsilon}$ with two independent coefficients.

$$\mathfrak{e}^T = \begin{bmatrix} 0 & 0 & e_{13} \\ 0 & 0 & e_{13} \\ 0 & 0 & e_{33} \\ 0 & 0 & 0 \\ e_{15} & 0 & 0 \\ 0 & e_{15} & 0 \end{bmatrix} \qquad \boldsymbol{\epsilon} = \begin{bmatrix} \epsilon_{11} & 0 & 0 \\ 0 & \epsilon_{11} & 0 \\ 0 & 0 & \epsilon_{33} \end{bmatrix} \tag{9}$$

For the shell, we derive the energy function W_s

$$W_s = \int_{\mathcal{B}_0} \frac{1}{2} \boldsymbol{\varepsilon}^T \boldsymbol{\sigma} \, \mathrm{d}V = \int_{\mathcal{B}_0} \frac{1}{2} \bar{\boldsymbol{\varepsilon}}^T \mathbf{A}^T \boldsymbol{\sigma} \, \mathrm{d}V = \int_{\Omega} \frac{1}{2} \bar{\boldsymbol{\varepsilon}}^T \underbrace{\int_{h_-}^{h_+} \boldsymbol{A}^T \boldsymbol{\sigma} \, \bar{\mu} d\xi^3}_{\bar{\boldsymbol{S}}} \, \mathrm{d}A \, . \tag{10}$$

Here, $\mathrm{d}V = \bar{\mu} \mathrm{d}\xi^3 \mathrm{d}A$ with the determinant of the shifter tensor $\bar{\mu}$. We obtain the stress resultants of the shell $\bar{\mathbf{S}}$ from the thickness integration. Applying the material law, the material matrix $\mathbb{D}$ of the shell arises from

$$\bar{\mathbf{S}} = \int_{h_-}^{h_+} \boldsymbol{A}^T \boldsymbol{\sigma} \, \bar{\mu} d\xi^3 \; = \underbrace{\int_{h_-}^{h_+} \boldsymbol{A}^T \bar{\mathbb{C}} \boldsymbol{A} \, \bar{\mu} d\xi^3}_{\mathbb{D}} \; \bar{\boldsymbol{\varepsilon}} \tag{11}$$

For slightly curved shells it holds $\bar{\mu} \approx 1$. Regarding layered structures we calculate $\mathbb{D}$ as the sum of the material matrix of every layer k as

$$\mathbb{D} = \sum_{k=1}^{n} \mathbb{D}_k = \sum_{k=1}^{n} \int_{h_{k-}}^{h_{k+}} \boldsymbol{A}^T \bar{\mathbb{C}}_{\boldsymbol{k}} \boldsymbol{A} \, \bar{\mu} d\xi^3 \quad . \tag{12}$$

The vector of the stress resultants has the form

$$\bar{\mathbf{S}} = [n^{11}, n^{22}, n^{12}, m^{11}, m^{22}, m^{12}, q^1, q^2, -d^1, -d^2, n_0^{33}, n_1^{33}, -d_0^3, -d_1^3]^T \tag{13}$$

with membrane forces $n^{\alpha\beta} = n^{\beta\alpha}$, bending moments $m^{\alpha\beta} = m^{\beta\alpha}$, shear forces q^α, and dielectric displacements d_α. $n_{0/1}^{33}$ and $d_{0/1}^3$ describe the constant and linear part of the components in thickness direction, respectively. The quantities $n^{\alpha\beta}$ and q^α are effective stress resultants, which are related to the integrals of the First Piola-Kirchhoff stress tensor by well known transformations. It holds $\mathbf{n}^\alpha := n^{\alpha\beta} \, \mathbf{x}_{,\beta} + q^\alpha \, \mathbf{d} + m^{\alpha\beta} \, \mathbf{d}_{,\beta}$, $\mathbf{m}^\alpha := \mathbf{d} \times m^{\alpha\beta} \, \mathbf{x}_{,\beta}$.
For the vector of the independent stress resultants and the independent dielectric displacements, we assume

$$\begin{aligned} \hat{\bar{\mathbf{S}}} &= \begin{bmatrix} n^{11} & n^{22} & n^{12} & m^1 & m^2 & m^{12} & q^1 & q^2 & -d^1 & -d^2 & 0 & 0 & 0 & 0 \end{bmatrix}^T \\ &= \begin{bmatrix} \hat{\mathbf{S}} & \underline{0} \end{bmatrix}^T \quad . \end{aligned} \tag{14}$$

The stress and dielectric displacement in thickness direction are defined as zero, thus we fulfill the normal zero stress condition of shells.

4 Ferroelectric hysteresis phenomena using the Preisach model

4.1 Nonlinear constitutive equations

Ferroelectric ceramics show strong nonlinear behavior under high electric fields. The imprinted initial polarization changes its direction under high electric loading and shows the dielectric hysteresis. Thus, the linear constitutive behavior according to (8) has to be set up under consideration of the current state of polarization. This state is characterized by the irreversible polarization $\vec{P}^i$. With the unit vector $\mathbf{e}^P$, the irreversible polarization vector $\vec{\mathbf{P}}^i$ yields to

$$\vec{\mathbf{P}}^i = \vec{P}^i \mathbf{e}^P, \qquad \vec{P}^i = \vec{P}^{sat} \vec{P}^{i,rel} \quad . \tag{15}$$

$\vec{P}^{sat}$ describes the saturation polarization and represents a material parameter. For the quantity of the relativ irreversible polarization $\vec{P}^{i,rel}$, it holds $-1 \leq \vec{P}^{i,rel} \leq 1$. $\vec{P}^{i,rel}$ characterizes the part of the piezoelectric material that shows a macroscopic polarization. We write the constitutive equations dependent of the state of polarization as

$$\begin{aligned} \mathbf{S} &= \mathbb{C} : (\mathbf{E} - \mathbf{E}^i) - \mathfrak{e}(\vec{\mathbf{P}}^i)\, \vec{\mathbf{E}} \\ -\vec{\mathbf{D}} + \vec{\mathbf{P}}^i &= -\mathfrak{e}^T(\vec{\mathbf{P}}^i) : (\mathbf{E} - \mathbf{E}^i) - \boldsymbol{\epsilon}\vec{\mathbf{E}} \quad . \end{aligned}$$

Since the switching effects of the ferroelectric domains can be treated as a volume conserving process, the irreversible strain $\mathbf{E}^i$ can be determined as proposed by Reference [25].

$$\mathbf{E}^i = \frac{3}{2} E^{sat} \frac{\|\vec{\mathbf{P}}^i\|}{\vec{P}^{sat}} (\vec{\mathbf{e}}^P \otimes \vec{\mathbf{e}}^P - \frac{1}{3}\mathbf{I}) \tag{16}$$

Here, E^{sat} defines the saturation strain of the ferroelectric material. According to Reference [26], the components of the polarization dependent piezoelectric modulus $\mathfrak{e}(\vec{\mathbf{P}}^i)$ can be calculated by

$$\begin{aligned} \mathfrak{e}_{kij} = \tfrac{\|\vec{\mathbf{P}}^i\|}{\vec{P}^{sat}} \; \{ & \mathfrak{e}_{\parallel} e_i^P e_j^P e_k^P && (17) \\ & + \mathfrak{e}_{\perp} (\delta_{ij} - e_i^P e_j^P) e_k^P && (18) \\ & + \mathfrak{e}_{=} \frac{1}{2} [(\delta_{ki} - e_k^P e_i^P) e_j^P + (\delta_{kj} - e_k^P e_j^P) e_i^P] \} \quad . && (19) \end{aligned}$$

$\mathfrak{e}_{\parallel}, \mathfrak{e}_{\perp}$ und $\mathfrak{e}_{=}$ correspond to the material parameters $\mathfrak{e}_{333}, \mathfrak{e}_{311}$ and $\mathfrak{e}_{131}$ for a completely poled material. In consideration of the symmetry, the tensor $\mathfrak{e}_{kij}$ can be transformed into the piezoelectric modulus $\mathfrak{e}$. Due to the isotropy, the elasticity matrix $\mathbb{C}$ and the permittivity matrix $\boldsymbol{\epsilon}$ are independent of the polarization state.

By means of the matrix $\mathbf{A}$, see (7), the polarization vector of the shell $\vec{\vec{\mathbf{P}}}^i$ reads

$$\vec{\vec{\mathbf{P}}}^i = \int_{h_-}^{h_+} \boldsymbol{A}^T \begin{bmatrix} \mathbf{0} \\ \vec{\mathbf{P}}^i \end{bmatrix} d\xi^3 \quad . \tag{20}$$

4.2 General description of the Preisach model

The Preisach model was introduced by F. Preisach [45], in order to analyze nonlinear behavior of ferromagnetic material. As a general mathematical model, it is able to describe various hysteresis curves of a wide range of different applications. For piezoelectric material behavior, the model was validated by Reference [46]. The basic idea of the Preisach model is that every hysteresis curve can be determined by an infinite number of unit hysteresis operators, see Figure 1, via superposition. These operators connect every input value $x(t)$ with an

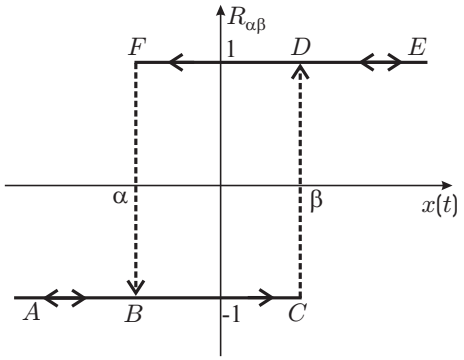

Figure 1: Unit hysteresis for the Preisach model.

output value $R_{\alpha\beta}(x(t))$, which can be $+1$ or -1. For a monotone increasing input value, the curve passes through ABCDE. In the case of a monotone decreasing value, it passes through EDFBA. For the specific up and down switching values α and β, it holds $\beta \geq \alpha$. The global output value $y(t)$ is obtained by superposition as

$$y(t) = \int_{\alpha} \int_{\beta} \mu(\alpha, \beta)\, R_{\alpha\beta}(x(t))\, \mathrm{d}\alpha\, \mathrm{d}\beta \quad . \tag{21}$$

Here, $\mu(\alpha, \beta)$ denotes the Preisach function, which represents a weighting function for each single hysteresis curve. For $\mu(\alpha, \beta)$ it is assumed

$$\int_{\alpha} \int_{\beta} \mu(\alpha, \beta)\, \mathrm{d}\alpha\, \mathrm{d}\beta = 1 \quad . \tag{22}$$

The constraint in (22) leads to the definition of the saturation value. The positive saturation of $y(t)$ is given as y^+, if all operators hold $R_{\alpha\beta}(x) = +1$. Vice versa for $R_{\alpha\beta}(x) = -1$ the negative saturation y^- is achieved with $y^+ = -y^-$.
A geometrical interpretation of the constraint $\beta \geq \alpha$ leads to a half plane T with the boundary line $\beta = \alpha$. Herein, each elementary hysteresis marks a point with (α, β). The pair of values (α_0, β_0), with α_0 and β_0 as the minimal and maximal switching values of α and β, respectively, reduce the half plane to a triangle, which is also called Preisach triangle. We assume that outside the triangle, the Preisach function vanishes, so it holds $\mu = 0$ for $(\alpha, \beta) \notin T$. Considering the loading history, that is the time variable input value, see Figure 2, the Preisach triangle can be partitioned, and we distinguish between S^+ as the intersection of all points where $R_{\alpha\beta}(x) = +1$, and S^- where $R_{\alpha\beta}(x) = -1$. Giving an initial configuration

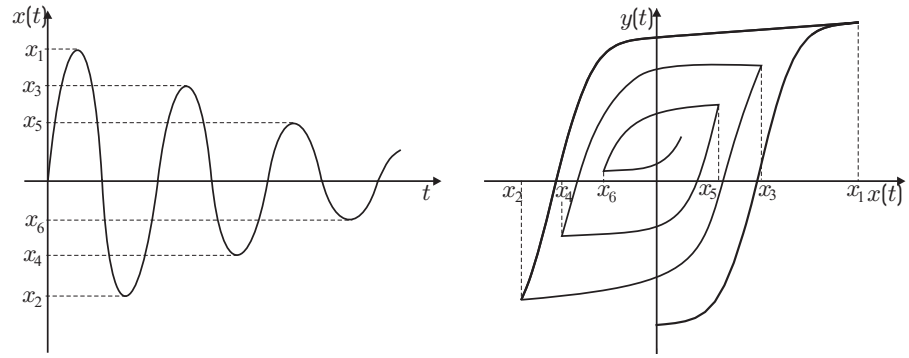

Figure 2: Preisach model.

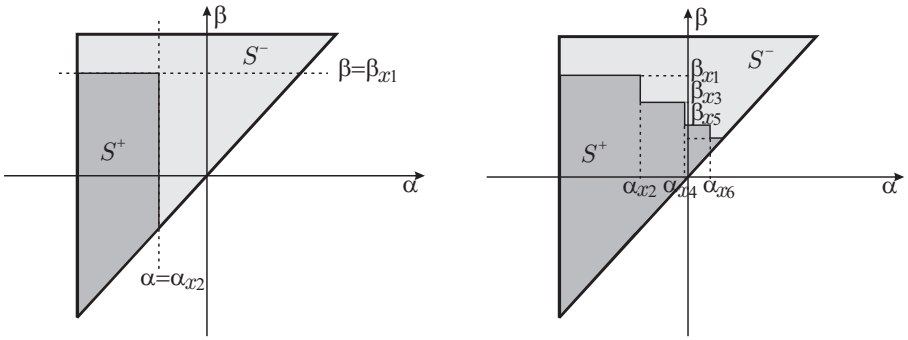

Figure 3: Preisach model.

with all operators count -1, the whole triangle is S^-. Increasing the input variable, some operators change to $+1$ and a partition S^+ arises, which is separated to S^- by a line $\beta = \beta_s$ parallel to the α axis, see Figure 3, until the local maximum $\beta = \beta_{x1}$ is reached. Decreasing input values lead to a vertical line with $\alpha = \alpha_s$ until the local minimum $\alpha = \alpha_{x2}$ comes up. Therefore, a loading history of local maxima and minima, as depicted in Figure 2, with $\beta_{x1} > \beta_{x3} > \beta_{x5}$ and $\alpha_{x2} < \alpha_{x4} < \alpha_{x6}$ respectively leads to a staircase function as shown in Figure 3. By means of the partitioned Preisach triangle, equation (21) can be written as

$$y(t) = \iint\limits_{S^+(t)} \mu(\alpha, \beta)\, \mathrm{d}\alpha\, \mathrm{d}\beta - \iint\limits_{S^-(t)} \mu(\alpha, \beta)\, \mathrm{d}\alpha\, \mathrm{d}\beta \quad . \tag{23}$$

Thus, the Preisach model permits to depict the loading history including subhysteresis curves, which is an essentiell advantage compared to other models. For a detailed description see e.g. Reference [47].

4.3 Interpretation for ferroelectric materials

To interpret the Preisach model for ferroelectric hysteresis phenomena, the input and output variables have to be identified. The loading parameter for piezoelectric devices is the electric field $\vec{\mathbf{E}}$. With the parameter of the material specific saturation value of the electric field $\vec{E}^{sat}$

the normalized value $\vec{E}^{rel}$ is chosen as

$$x(t) = \vec{E}^{rel} = \frac{\|\vec{\mathbf{E}}\|}{\vec{E}^{sat}} \quad . \tag{24}$$

The corresponding output quantity is chosen as the normalized polarization $\vec{P}^{i,rel}$

$$y(t) = \vec{P}^{i,rel} = \frac{\|\vec{\mathbf{P}}^{i}\|}{\vec{P}^{sat}} \tag{25}$$

with the material parameter of the saturation polarization $\vec{P}^{sat}$. As a phenomenological model, the Preisach concept adjusts the final hysteresis form by means of an experimental determined function. According to Reference [48] we choose the weighting function μ

$$\mu = c \cdot e^{-f_\alpha(\alpha-\beta-y_\alpha+y_\beta)^2-f_\beta(\alpha+\beta-y_\alpha-y_\beta)^2} \quad . \tag{26}$$

The parameters c, f_α, f_β, y_α, and y_β are set up from experimental data. For a detailed description and a discussion regarding the choice of the Preisach function see e.g. References [49, 50, 47, 51]. It is remarked that the polarization output value denotes the normalized irreversible polarization. Therefore, it results a horizontal line of the hysteresis function above the saturation. Actually the reversible polarization has to be added, which holds according to Reference [26]

$$\vec{\mathbf{P}}^{r} = \boldsymbol{\kappa}\vec{\mathbf{E}} + \mathfrak{d} : \mathbf{S} \quad . \tag{27}$$

$\boldsymbol{\kappa}$ represents the susceptibility and $\mathfrak{d}$ the piezoelectric coupling module with $\mathfrak{d} = \mathbb{C}^{-1}\mathfrak{e}$.

4.4 Temperature-dependent hysteresis

The influence of the temperature on the saturation parameter of the polarization P^{sat} and the electric coercitive field E_c has been experimentally studied by Reference [37] for $Pb(Zn_{1/3}Nb_{2/3})O_3-PbTiO_3$ single crystals and by Reference [38] for PZT ceramics. With increasing temperature, the domain walls start moving earlier and the hysteresis area decreases. Following the experimental investigations in Reference [39] we assume a linear relation between the natural logarithms of the temperature and the saturation polarization. With the experimental data from [38] for the material PZT we include the phenomenological saturation parameter

$$P^{sat} = exp\left(10.305 \ T^{-1.2322}\,[K]\right) \quad . \tag{28}$$

Note that the temperature in this equation is of unit Kelvin. We assume that also the saturation strain depends on the temperature. As there do not exist sufficient test results, this influence has been neglected.
Based on Reference [38] we include the relation

$$E_c = -0.03085 \ T\,[K] + 18.319 \tag{29}$$

for the coercitive field. For the numerical investigation, we assume that the temperature remains under the Curie temperature, where the polarization vanishes with the transition to the paraelectric phase.

5 Variational formulation

The variation of the generalized geometric vector $\delta\boldsymbol{\varepsilon}_g$ can be written as $\delta\boldsymbol{\varepsilon}_g = [\delta\varepsilon_{11}, \delta\varepsilon_{22}, 2\delta\varepsilon_{12}, \delta\kappa_{11}, \delta\kappa_{22}, 2\delta$ with

$$\begin{aligned}
\delta\varepsilon_{\alpha\beta} &= \frac{1}{2}(\delta\mathbf{x}_{,\alpha}\cdot\mathbf{x}_{,\beta} + \delta\mathbf{x}_{,\beta}\cdot\mathbf{x}_{,\alpha}) \\
\delta\kappa_{\alpha\beta} &= \frac{1}{2}(\delta\mathbf{x}_{,\alpha}\cdot\mathbf{d}_{,\beta} + \delta\mathbf{x}_{,\beta}\cdot\mathbf{d}_{,\alpha} + \delta\mathbf{d}_{,\alpha}\cdot\mathbf{x}_{,\beta} + \delta\mathbf{d}_{,\beta}\cdot\mathbf{x}_{,\alpha}) \\
\delta\gamma_{\alpha} &= \delta\mathbf{x}_{,\alpha}\cdot\mathbf{d} + \delta\mathbf{d}\cdot\mathbf{x}_{,\alpha} \\
\delta\vec{E}_{\alpha} &= -\delta(\Delta\varphi)_{,\alpha}
\end{aligned} \tag{30}$$

Referring to (6), it holds $\delta\boldsymbol{\varepsilon} = \mathbf{A}\delta\bar{\boldsymbol{\varepsilon}}$. We postulate the existence of the strain energy function $\hat{W}(\mathbf{C})$ and write the internal virtual work of the shell as

$$\delta W_i = \int_{\Omega}\int_{h} \delta\hat{W}(\mathbf{C})\bar{\mu}\,\mathrm{d}\xi^3\,dA = \int_{\Omega} \delta\boldsymbol{\varepsilon}^T\partial_{\boldsymbol{\varepsilon}}W\,dA \quad . \tag{31}$$

Here, $\mathrm{d}A = j\mathrm{d}\xi^1\mathrm{d}\xi^2$ is the area element with $j(\xi,\eta) = |\mathbf{X}^h_{,\xi}\times\mathbf{X}^h_{,\eta}|$. Considering $\delta\hat{W}(\mathbf{C}) = 2\delta\boldsymbol{\varepsilon} : \partial_{\mathbf{C}}\hat{W}(\mathbf{C}) = (\mathbf{A}\delta\boldsymbol{\varepsilon}) : 2\partial_{\mathbf{C}}\hat{W}(\mathbf{C})$, we obtain the vector of the stress resultants

$$\partial_{\boldsymbol{\varepsilon}}W = \int_{h_-}^{h_+} \mathbf{A}^T\boldsymbol{\sigma}\bar{\mu}\,\mathrm{d}\xi^3 \quad . \tag{32}$$

The generalized stress tensor $\boldsymbol{\sigma}$ containing the second Piola-Kirchhoff stresses reads $\boldsymbol{\sigma} = 2\partial_{\mathbf{C}}\hat{W}(\mathbf{C})$. In the following, we summarize the static and geometric field equations as well as the constitutive equations in $\boldsymbol{\Omega}$

$$\frac{1}{j}(j\mathbf{n}^{\alpha})_{,\alpha} + \bar{\mathbf{b}} = \mathbf{0} \qquad \boldsymbol{\varepsilon}_g - \hat{\boldsymbol{\varepsilon}} = \mathbf{0} \tag{33}$$

$$\frac{1}{j}(j\mathbf{m}^{\alpha})_{,\alpha} + \mathbf{x}\times\mathbf{n}^{\alpha} = \mathbf{0} \qquad \partial_{\hat{\hat{\boldsymbol{\varepsilon}}}}W - \hat{\hat{\mathbf{S}}} = \mathbf{0} \quad . \tag{34}$$

$\bar{\mathbf{b}}$ represents the surface loads on Ω. Displacements $\mathbf{u}$, rotations $\boldsymbol{\omega}$ and an electric potential $\Delta\varphi$ summarized in the vector $\mathbf{v} = [\mathbf{u}, \boldsymbol{\omega}, \Delta\varphi]^T$ can be prescribed on Γ_u by $\bar{\mathbf{v}}$, where $\Gamma = \Gamma_\sigma \bigcup \Gamma_u$. With the boundary loads $\bar{\mathbf{t}}$ on Γ_σ, the static and geometric boundary conditions read

$$j(\mathbf{n}^{\alpha}\nu_{\alpha}) - \bar{\mathbf{t}} = \mathbf{0} \quad \text{on} \quad \Gamma_\sigma \tag{35}$$

$$\mathbf{v} - \bar{\mathbf{v}} = \mathbf{0} \quad \text{on} \quad \Gamma_u \quad . \tag{36}$$

ν_α denotes the components of the normal vector on the shell boundary. The virtual quantities of $\mathbf{v}$ and the independently assumed strains, electric field, stresses, and dielectric displacements summarized in the generalized electromechanic fields $\hat{\boldsymbol{\varepsilon}}(\hat{\mathbf{E}}, \hat{\vec{\mathbf{E}}})$ and $\hat{\boldsymbol{\sigma}}(\hat{\mathbf{S}}, \hat{\vec{\mathbf{D}}})$ arrive to $\delta\mathbf{v}(\delta\mathbf{u}, \delta\boldsymbol{\omega}, \delta\Delta\varphi)$, $\delta\hat{\boldsymbol{\varepsilon}}(\delta\hat{\mathbf{E}}, \delta\hat{\vec{\mathbf{E}}})$ and $\delta\hat{\boldsymbol{\sigma}}(\delta\hat{\mathbf{S}}, \delta\hat{\vec{\mathbf{D}}})$.
We introduce $\boldsymbol{\theta}[\mathbf{v}, \hat{\boldsymbol{\varepsilon}}, \hat{\boldsymbol{\sigma}}]^T$ with $\delta\boldsymbol{\theta}[\delta\mathbf{v}, \delta\hat{\boldsymbol{\varepsilon}}, \delta\hat{\boldsymbol{\sigma}}]^T$ and formulate the weak form of the boundary

value problem in the standard way

$$
\begin{aligned}
G(\boldsymbol{\theta}, \delta\boldsymbol{\theta}) &= \int_{\Omega} \left[\delta\hat{\bar{\boldsymbol{\varepsilon}}}^T (\partial_{\hat{\bar{\boldsymbol{\varepsilon}}}} W - \hat{\bar{\mathbf{S}}}) + \delta\hat{\mathbf{S}}^T (\boldsymbol{\varepsilon}_g - \hat{\boldsymbol{\varepsilon}}) \right] dA \\
&- \int_{\Omega} \left[\left(\frac{1}{j} (j\mathbf{n}^\alpha)_{,\alpha} + \bar{\mathbf{b}} \right) \cdot \delta\mathbf{v} + \left(\frac{1}{j} (j\mathbf{m}^\alpha)_{,\alpha} + \mathbf{x} \times \mathbf{n}^\alpha \right) \cdot \delta\boldsymbol{\omega} \right] dA = 0 \quad .
\end{aligned}
\tag{37}
$$

Integration by parts of the second integral and the incorporation of the static boundary conditions yields

$$
\begin{aligned}
G(\boldsymbol{\theta}, \delta\boldsymbol{\theta}) &= \int_{\Omega} \left[\delta\hat{\bar{\boldsymbol{\varepsilon}}}^T (\partial_{\hat{\bar{\boldsymbol{\varepsilon}}}} W - \hat{\bar{\mathbf{S}}}) + \delta\hat{\mathbf{S}}^T (\boldsymbol{\varepsilon}_g - \hat{\boldsymbol{\varepsilon}}) + \delta\boldsymbol{\varepsilon}_g^T \hat{\mathbf{S}} \right] dA \\
&- \int_{\Omega} \delta\mathbf{v}^T \bar{\mathbf{b}} \, dA - \int_{\Gamma_\sigma} \delta\mathbf{v}^T \bar{\mathbf{t}} \, ds = 0 \quad .
\end{aligned}
\tag{38}
$$

6 Finite element approximation

The finite element formulation models the shell structure by a reference surface. We choose a four node element with bilinear shape functions N_I

$$
N_I(\xi, \eta) = \frac{1}{4}(1 + \xi_I \xi)(1 + \eta_I \eta) \qquad I = 1..4 \quad . \tag{39}
$$

Regarding the geometry, we approximate the position vector and the director vector by

$$
\mathbf{X}^h = \sum_{I=1}^{4} N_I \, \mathbf{X}_I \qquad \mathbf{D}^h = \sum_{I=1}^{4} N_I \, \mathbf{D}_I \quad . \tag{40}
$$

The local numbering of the nodes and the midside points are shown in Figure 4. The coordinates $\{\xi, \eta\} \in [-1, 1]$ are mapped from the unit square on the reference surface in the reference and the current configuration. It holds $\xi_I \in \{-1, \quad 1, \quad 1, -1\}$ and $\eta_I \in \{-1, -1, \quad 1, \quad 1\}$. The superscript h denotes the characteristic size of the element discretisation and indicates the finite element approximation. The nodal position vector $\mathbf{X}_I$ and the local cartesian coordinate system $[\mathbf{A}_{1I}, \mathbf{A}_{2I}, \mathbf{A}_{3I}]$ are generated with the mesh input. Here $\mathbf{D}_I = \mathbf{A}_{3I}$ is set perpendicular to the surface Ω and $\mathbf{A}_{1I}$, $\mathbf{A}_{2I}$ are built fulfilling the boundary conditions. It should be remarked that the orthogonality holds true only for the nodal points. For every element we calculate a local cartesian basis system $\mathbf{t}_i$ according to Reference [52]. Here, $\mathbf{t}_3$ represents the normal vector in the midpoint of the element. $\mathbf{t}_1$ and $\mathbf{t}_2$ span the tangent plane in the element midpoint. The reference surface in the current configuration is approximated by the position vector $\mathbf{x}^h$ and the director vector $\mathbf{d}^h$ with

$$
\mathbf{x}^h = \sum_{I=1}^{4} N_I \, \mathbf{x}_I \qquad \mathbf{d}^h = \sum_{I=1}^{4} N_I \, \mathbf{d}_I \quad . \tag{41}
$$

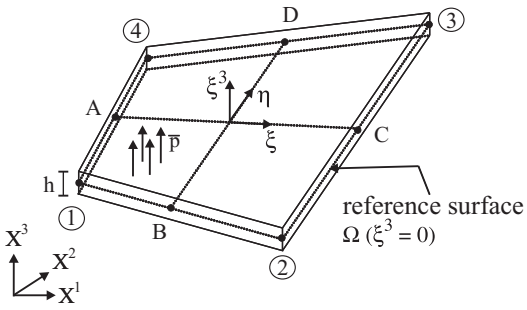

Figure 4: Four node shell element.

For every node $\mathbf{x}_I = \mathbf{X}_I + \mathbf{u}_I$ characterizes the position vector in the current configuration and we obtain $\mathbf{d}_I = \mathbf{a}_{3I}$ by the orthogonal transformation $\mathbf{a}_{kI} = \mathbf{R}_I\,\mathbf{A}_{kI}$ with $k = 1, 2, 3$. The rotational parameters ω_{kI} are arranged in the vector $\boldsymbol{\omega}_I = [\omega_{1I}, \omega_{2I}, \omega_{3I}]^T$. The rotation tensor $\mathbf{R}_I$ as a function of the parameters ω_{kI} is calculated via the Rodrigues' formula

$$\mathbf{R}_I = \mathbf{1} + \frac{\sin\omega_I}{\omega_I}\boldsymbol{\Omega}_I + \frac{1-\cos\omega_I}{\omega_I^2}\boldsymbol{\Omega}_I^2 \qquad \boldsymbol{\Omega}_I = \operatorname{skew}\boldsymbol{\omega}_I = \begin{bmatrix} 0 & -\omega_{3I} & \omega_{2I} \\ \omega_{3I} & 0 & -\omega_{1I} \\ -\omega_{2I} & \omega_{1I} & 0 \end{bmatrix} \quad . \tag{42}$$

Equation (42) is free of singularities for $\omega_I = |\boldsymbol{\omega}_I| < 2\pi$, which is always fulfilled if a multiplicative update of the total rotation tensor is applied after a certain number of load steps. We assume that the shell structure only counts for an electric potential in thickness direction of the shell by means of electrodes on the upper and lower surface of the shell. With an initial polarization of the piezoelectric material in thickness direction, the difference of the electric potential in thickness direction $\Delta\varphi$ is assumed to be the only electrical degree of freedom at each element node. Thus, the nodal degrees of freedom are three local displacements, three local rotations, and the difference of the electric potential. By means of the isoparametric concept, the geometry as well as the displacements $\mathbf{u}^h$ and the electric potential $\Delta\varphi^h$ are approximated on element level by the same shape functions N_I.

$$\mathbf{u}^h = \sum_{I=1}^{4} N_I\,\mathbf{u}_I \qquad \Delta\varphi^h = \sum_{I=1}^{4} N_I\,\Delta\varphi_I \tag{43}$$

Summarizing (43) we write

$$\begin{bmatrix} \mathbf{u}^h \\ \Delta\varphi^h \end{bmatrix} = \sum_{I=1}^{4} N_I\,\mathbf{v}_I = \mathbf{N}\,\mathbf{v}_e \qquad \text{with } \mathbf{v}_e^T = [\mathbf{v}_1^T \quad \mathbf{v}_2^T \quad \mathbf{v}_3^T \quad \mathbf{v}_4^T] \tag{44}$$

and $\mathbf{v}_I = (u_1 \quad u_2 \quad u_3 \quad \omega_1 \quad \omega_2 \quad \omega_3 \quad \Delta\varphi)_I$. We approximate the generalized variational vector of the geometric strain and the geometric electric field $\delta\boldsymbol{\varepsilon}_g$ by means of the matrix $\mathbf{B}$

$$\delta\boldsymbol{\varepsilon}_g = \sum_{I=1}^{4} \mathbf{B}_I\,\delta\mathbf{v}_I = \mathbf{B}\,\delta\mathbf{v}_e \quad . \tag{45}$$

The element has to fulfill the patch tests. In order to fulfill the bending patch test, the shear strains based on linear displacement interpolations in $(3)_3$ has to be substituted by the

strains defined in Reference [53] to avoid shear locking phenomena. Thus, we formulate the approximation of the shell strains as

$$\boldsymbol{\varepsilon}_g^h = \begin{bmatrix} \varepsilon_{11}^h \\ \varepsilon_{22}^h \\ 2\varepsilon_{12}^h \\ \kappa_{11}^h \\ \kappa_{22}^h \\ 2\kappa_{12}^h \\ \gamma_1^h \\ \gamma_2^h \\ \vec{E}_1 \\ \vec{E}_2 \end{bmatrix} = \begin{bmatrix} \frac{1}{2}\left(\mathbf{x}_{,1}^h \cdot \mathbf{x}_{,1}^h - \mathbf{X}_{,1}^h \cdot \mathbf{X}_{,1}^h\right) \\ \frac{1}{2}\left(\mathbf{x}_{,2}^h \cdot \mathbf{x}_{,2}^h - \mathbf{X}_{,2}^h \cdot \mathbf{X}_{,2}^h\right) \\ \mathbf{x}_{,1}^h \cdot \mathbf{x}_{,2}^h - \mathbf{X}_{,1}^h \cdot \mathbf{X}_{,2}^h \\ \mathbf{x}_{,1}^h \cdot \mathbf{d}_{,1}^h - \mathbf{X}_{,1}^h \cdot \mathbf{D}_{,1}^h \\ \mathbf{x}_{,2}^h \cdot \mathbf{d}_{,2}^h - \mathbf{X}_{,2}^h \cdot \mathbf{D}_{,2}^h \\ \mathbf{x}_{,1}^h \cdot \mathbf{d}_{,2}^h + \mathbf{x}_{,2}^h \cdot \mathbf{d}_{,1}^h - \mathbf{X}_{,1}^h \cdot \mathbf{D}_{,2}^h - \mathbf{X}_{,2}^h \cdot \mathbf{D}_{,1}^h \\ \mathbf{J}^{-1} \begin{Bmatrix} \frac{1}{2}[(1-\eta)\,\gamma_\xi^B + (1+\eta)\,\gamma_\xi^D \\ \frac{1}{2}[(1-\xi)\,\gamma_\eta^A + (1+\xi)\,\gamma_\eta^C] \end{Bmatrix} \\ \mathbf{J}^{-1} \cdot \mathbf{N}_{\vec{E}} \begin{Bmatrix} \Delta\varphi \\ \Delta\varphi \end{Bmatrix} \end{bmatrix} . \tag{46}$$

with $\mathbf{N}_{\vec{E}} = \begin{bmatrix} N_{,\xi} & N_{,\eta} \end{bmatrix}^T$. $\mathbf{J}$ here denotes the Jacobian matrix. The strains referring to the midside nodes A, B, C, D of the element read

$$\begin{aligned} \gamma_\xi^M &= [\mathbf{x}_{,\xi} \cdot \mathbf{d} - \mathbf{X}_{,\xi} \cdot \mathbf{D}]^M \qquad M = B, D \\ \gamma_\eta^L &= [\mathbf{x}_{,\eta} \cdot \mathbf{d} - \mathbf{X}_{,\eta} \cdot \mathbf{D}]^L \qquad L = A, C \quad . \end{aligned} \tag{47}$$

For a detailed description of the derivatives of the position and director vectors see Reference [55].

6.1 Interpolation of the assumed strains and electric field

The independent fields of the strains and the electric field are interpolated by

$$\hat{\bar{\boldsymbol{\varepsilon}}} = \bar{\mathbf{N}}_\varepsilon \, \bar{\boldsymbol{\alpha}}, \qquad \hat{\boldsymbol{\varepsilon}} = \hat{\mathbf{N}}_\varepsilon \, \boldsymbol{\alpha} \tag{48}$$

Here $\hat{\bar{\boldsymbol{\varepsilon}}}$ characterizes the complete vector of the assumed strains and the assumed electric fields, whereas $\hat{\boldsymbol{\varepsilon}}$ specifies the reduced vector without the components in thickness direction. $\bar{\boldsymbol{\alpha}}$ and $\boldsymbol{\alpha}$ contain independent variables, which can be eliminated by static condensation on element level. We define the matrices $\bar{\mathbf{N}}_\varepsilon$ and $\hat{\mathbf{N}}_\varepsilon$ as

$$
\begin{aligned}
\hat{\mathbf{N}}_\varepsilon &= \begin{bmatrix} \mathbf{N}_\varepsilon & \underline{0} \\ \underline{0} & \mathbf{N}_\varepsilon^{el} \end{bmatrix} \\
\bar{\mathbf{N}}_\varepsilon &= \begin{bmatrix} \hat{\mathbf{N}}_\varepsilon & \underline{0} & \underline{0} & \mathbf{N}_{eas} \\ \underline{0} & \mathbf{N}_\varepsilon^z & \underline{0} & \underline{0} \\ \underline{0} & \underline{0} & \tilde{\mathbf{N}}_\varepsilon^{el} & \underline{0} \end{bmatrix}
\end{aligned}
\qquad
\begin{aligned}
\mathbf{N}_\varepsilon &= \begin{bmatrix} \mathbf{1}_3 & \underline{0} & \underline{0} & \mathbf{N}_\varepsilon^m & \underline{0} & \underline{0} \\ \underline{0} & \mathbf{1}_3 & \underline{0} & \underline{0} & \mathbf{N}_\varepsilon^b & \underline{0} \\ \underline{0} & \underline{0} & \mathbf{1}_2 & \underline{0} & \underline{0} & \mathbf{N}_\varepsilon^s \end{bmatrix} \\
\mathbf{N}_\varepsilon^{el} &= \mathbf{J} \begin{bmatrix} 1 & 0 & \tilde{\eta} & 0 \\ 0 & 1 & 0 & \tilde{\xi} \end{bmatrix} \\
\mathbf{N}_\varepsilon^z &= \begin{bmatrix} 1 & 0 & \tilde{\xi} & \tilde{\eta} & \tilde{\xi}\cdot\tilde{\eta} & 0 & 0 & 0 \\ 0 & 1 & 0 & 0 & 0 & \tilde{\xi} & \tilde{\eta} & \tilde{\xi}\cdot\tilde{\eta} \end{bmatrix} \\
\tilde{\mathbf{N}}_\varepsilon^{el} &= \mathbf{J} \begin{bmatrix} 1 & 0 & \tilde{\xi} & \tilde{\eta} & \tilde{\xi}\cdot\tilde{\eta} & 0 & 0 & 0 \\ 0 & 1 & 0 & 0 & 0 & \tilde{\xi} & \tilde{\eta} & \tilde{\xi}\cdot\tilde{\eta} \end{bmatrix} .
\end{aligned}
\tag{49}
$$

It holds $\tilde{\xi} = \xi - \bar{\xi}$ and $\tilde{\eta} = \eta - \bar{\eta}$. Due to the constants $\bar{\xi}$ and $\bar{\eta}$

$$
\bar{\xi} = \frac{1}{A_e} \int_{\Omega_e} \xi \, dA \qquad \bar{\eta} = \frac{1}{A_e} \int_{\Omega_e} \eta \, dA \qquad A_e = \int_{\Omega_e} dA \tag{50}
$$

the orthogonality between the linear and the constant functions is given, which yields partly decoupled matrices. The area element $dA = j \, d\xi d\eta$ is given with $j(\xi, \eta) = |\mathbf{X}^h_{,\xi} \times \mathbf{X}^h_{,\eta}|$.
The matrix $\mathbf{N}_{eas}$ contains parameters that are set orthogonal to the interpolations of the stresses, which is similar to the enhanced strain formulation given by Reference [54]. We define $\mathbf{N}_{eas}$ as

$$
\begin{aligned}
\mathbf{N}_{eas} &= \begin{bmatrix} \mathbf{N}_{eas}^m & \underline{0} \\ \underline{0} & \mathbf{N}_{eas}^b \end{bmatrix} \qquad & \mathbf{N}_{eas}^m &= \mathbf{N}_{eas}^b = \tfrac{j_0}{j} (\mathbf{T}_\sigma^0)^{-T} \mathbf{M}_\alpha \\
\mathbf{M}_\alpha &= \begin{bmatrix} \xi & 0 & \xi\eta & 0 & 0 & 0 & 0 \\ 0 & \eta & 0 & \xi\eta & 0 & 0 & 0 \\ 0 & 0 & 0 & 0 & \xi & \eta & \xi\eta \end{bmatrix} \qquad & \alpha &= 2, 4, 7 \quad .
\end{aligned}
\tag{51}
$$

The matrix $\mathbf{T}_\sigma^0$ is specified in (56). According to Reference [55], the matrices $\mathbf{N}_\varepsilon^m$, $\mathbf{N}_\varepsilon^b$ und $\mathbf{N}_\varepsilon^s$ are defined as

$$
\mathbf{N}_\varepsilon^m = \mathbf{N}_\varepsilon^b = \mathbf{T}_\varepsilon^0 \begin{bmatrix} \tilde{\eta} & 0 \\ 0 & \tilde{\xi} \\ 0 & 0 \end{bmatrix} , \quad \mathbf{T}_\varepsilon^0 = \begin{bmatrix} J_{11}^0 J_{11}^0 & J_{21}^0 J_{21}^0 & J_{11}^0 J_{21}^0 \\ J_{12}^0 J_{12}^0 & J_{22}^0 J_{22}^0 & J_{12}^0 J_{22}^0 \\ 2 J_{11}^0 J_{12}^0 & 2 J_{21}^0 J_{22}^0 & J_{11}^0 J_{22}^0 + J_{12}^0 J_{21}^0 \end{bmatrix} \tag{52}
$$

$$
\mathbf{N}_\varepsilon^s = \tilde{\mathbf{T}}_\varepsilon^0 \begin{bmatrix} \tilde{\eta} & 0 \\ 0 & \tilde{\xi} \end{bmatrix} , \quad \tilde{\mathbf{T}}_\varepsilon^0 = \begin{bmatrix} J_{11}^0 & J_{21}^0 \\ J_{12}^0 & J_{22}^0 \end{bmatrix} \quad . \tag{53}
$$

The transformation of the contravariant tensor components into a cartesian coordinate system related to the element center is described by $\mathbf{T}_\varepsilon^0$ and $\tilde{\mathbf{T}}_\varepsilon^0$. The constants $J_{\alpha\beta}^0 = J_{\alpha\beta}(\xi = 0, \eta = 0)$ are the components of the Jacobian matrix $\mathbf{J}$ evaluated in the element center.

6.2 Interpolation of the assumed stresses and dielectric displacements

The vector of the independent stress resultants and the independent dielectric displacements without the components in thickness direction $\hat{\mathbf{S}}$ is given as

$$\hat{\mathbf{S}} = \mathbf{N}_\sigma \, \boldsymbol{\beta} \tag{54}$$

with the vector $\boldsymbol{\beta}$ containing independent variables. The matrix $\mathbf{N}_\sigma$ is defined as

$$\mathbf{N}_\sigma = \begin{bmatrix} \mathbf{N}_\sigma^{mech} & \underline{0} \\ \underline{0} & \mathbf{N}_\sigma^{el} \end{bmatrix} \qquad \mathbf{N}_\sigma^{mech} = \begin{bmatrix} \mathbf{1}_3 & \underline{0} & \underline{0} & \mathbf{N}_\sigma^m & \underline{0} & \underline{0} \\ \underline{0} & \mathbf{1}_3 & \underline{0} & \underline{0} & \mathbf{N}_\sigma^b & \underline{0} \\ \underline{0} & \underline{0} & \mathbf{1}_2 & \underline{0} & \underline{0} & \mathbf{N}_\sigma^s \end{bmatrix}$$

$$\mathbf{N}_\sigma^{el} = \mathbf{N}_\varepsilon^{el} \tag{55}$$

with the matrices

$$\mathbf{N}_\sigma^m = \mathbf{N}_\sigma^b = \mathbf{T}_\sigma^0 \begin{bmatrix} \tilde{\eta} & 0 \\ 0 & \tilde{\xi} \\ 0 & 0 \end{bmatrix}, \quad \mathbf{T}_\sigma^0 = \begin{bmatrix} J_{11}^0 J_{11}^0 & J_{21}^0 J_{21}^0 & 2 J_{11}^0 J_{21}^0 \\ J_{12}^0 J_{12}^0 & J_{22}^0 J_{22}^0 & 2 J_{12}^0 J_{22}^0 \\ J_{11}^0 J_{12}^0 & J_{21}^0 J_{22}^0 & J_{11}^0 J_{22}^0 + J_{12}^0 J_{21}^0 \end{bmatrix} \tag{56}$$

$$\mathbf{N}_\sigma^s = \mathbf{N}_\varepsilon^s \quad . \tag{57}$$

The interpolation of the membrane and bending strains corresponds to the procedure introduced by Reference [56]. For $\bar{\xi} = \bar{\eta} = 0$, the plane strain problem according to Reference [57] is solved.

6.3 Approximation of the weak form and linearization

According to equation (38) the approximation of the variational formulation reads

$$\begin{aligned} G(\boldsymbol{\theta}, \delta\boldsymbol{\theta}) = & \int_{\Omega} \left[\delta\boldsymbol{\varepsilon}_g^T \, \hat{\mathbf{S}} - \delta\mathbf{v}^T \, \bar{\mathbf{b}} \right] dA - \int_{\Gamma_\sigma} \delta\mathbf{v}^T \, \bar{\mathbf{t}} \, ds \\ & + \int_{\Omega} \delta\hat{\bar{\boldsymbol{\varepsilon}}}^T (\partial_{\hat{\bar{\boldsymbol{\varepsilon}}}} W - \hat{\bar{\mathbf{S}}}) \, dA \\ & + \int_{\Omega} \delta\hat{\mathbf{S}}^T \, (\boldsymbol{\varepsilon}_g - \hat{\boldsymbol{\varepsilon}}) \, dA \qquad = 0 \end{aligned} \tag{58}$$

including the variational quantities of the assumed strains and the assumed electric field with and without the thickness components $\delta\hat{\bar{\boldsymbol{\varepsilon}}}$ and $\delta\hat{\boldsymbol{\varepsilon}}$, respectively, as well as the variational tensor of the stress resultants and the dielectric displacement $\delta\hat{\mathbf{S}}$. For these variational components, it holds

$$\delta\hat{\bar{\boldsymbol{\varepsilon}}} = \bar{\mathbf{N}}_\varepsilon \, \delta\bar{\boldsymbol{\alpha}}_e \qquad \delta\hat{\boldsymbol{\varepsilon}} = \hat{\mathbf{N}}_\varepsilon \, \delta\boldsymbol{\alpha}_e \qquad \delta\hat{\mathbf{S}} = \mathbf{N}_\sigma \, \delta\boldsymbol{\beta}_e \quad . \tag{59}$$

We incorporate the interpolations of the strains, the electric fields, the stress resultants, and the dielectric displacements in equation (58) and formulate the approximation of the variational formulation on element level as

$$
\begin{aligned}
G(\boldsymbol{\theta}, \delta\boldsymbol{\theta}) = \delta \mathbf{v}_e^T & \int_{\boldsymbol{\Omega}_e} \left[\mathbf{B}^T \mathbf{N}_\sigma \ \boldsymbol{\beta} - \boldsymbol{f}^{\boldsymbol{a}} \right] \, dA \\
& + \delta \bar{\boldsymbol{\alpha}}_e^T \int_{\boldsymbol{\Omega}_e} \left[\bar{\mathbf{N}}_\varepsilon^T \partial_{\hat{\boldsymbol{\varepsilon}}} W \right] \, dA - \delta \boldsymbol{\alpha}_e^T \int_{\boldsymbol{\Omega}_e} \left[\hat{\mathbf{N}}_\varepsilon^T \mathbf{N}_\sigma \, \boldsymbol{\beta} \right] \, dA \\
& + \delta \boldsymbol{\beta}_e^T \int_{\boldsymbol{\Omega}_e} \left[\mathbf{N}_\sigma^T \boldsymbol{\varepsilon}_g - \mathbf{N}_\sigma^T \hat{\mathbf{N}}_\varepsilon \ \boldsymbol{\alpha} \right] \, dA \quad .
\end{aligned} \tag{60}
$$

The external loads are summarized in $\mathbf{f}^a$. Considering nonlinear structural and material behavior, this formulation has to be linearized. With the material matrix $\mathbb{D}$

$$
\mathbb{D} := \partial^2_{\hat{\boldsymbol{\varepsilon}}} W = \int_{h_-}^{h_+} \mathbf{A}^T 4 \frac{\partial^2 \hat{W}(\mathbf{C})}{\partial \mathbf{C} \, \partial \mathbf{C}} \mathbf{A} \, \bar{\mu} \, d\xi^3 \tag{61}
$$

the linearized variational formulation is given by

$$
\begin{aligned}
& L\left[G(\boldsymbol{\theta}, \delta\boldsymbol{\theta}), \Delta\boldsymbol{\theta}\right] := G(\boldsymbol{\theta}, \delta\boldsymbol{\theta}) + D\, G \cdot \Delta\boldsymbol{\theta} = 0 \\
& D\, G \cdot \Delta\boldsymbol{\theta} = \int_{\Omega_e} [\delta\boldsymbol{\varepsilon}_g^T \Delta\hat{\boldsymbol{S}} + \delta\Delta\boldsymbol{\varepsilon}_g^T \hat{\boldsymbol{S}} + \delta\hat{\bar{\boldsymbol{\varepsilon}}}^T (\mathbb{D}\Delta\hat{\bar{\boldsymbol{\varepsilon}}} + \Delta\vec{\mathbf{P}}^i - \Delta\hat{\bar{\boldsymbol{S}}}) + \delta\hat{\boldsymbol{S}}^T (\Delta\boldsymbol{\varepsilon}_g - \Delta\hat{\boldsymbol{\varepsilon}})] \, dA \quad .
\end{aligned} \tag{62}
$$

The integration over the thickness in (61) is numerically solved by the sum over all layers, with two Gauss integration points for each layer. The irreversible polarization is a function of the electric field. The linearized part of the polarization $\Delta\vec{\mathbf{P}}^i$ yields

$$
\Delta\vec{\mathbf{P}}^i = \frac{\partial\vec{\mathbf{P}}^i}{\partial\vec{\mathbf{E}}} \Delta\vec{\mathbf{E}} \quad . \tag{63}
$$

The partial derivative of the irreversible polarization with respect to the electric field can be interpreted as an additional portion of the electrical permittivity

$$
\boldsymbol{\epsilon}^P = \frac{\partial\vec{\mathbf{P}}^i}{\partial\vec{\mathbf{E}}} \quad . \tag{64}
$$

Thus, the polarization vector in the constitutive equations can be substituted for the additional permittivity part $\Delta\vec{\mathbf{P}}^i = \boldsymbol{\epsilon}^P \, \Delta\vec{\mathbf{E}}$, which we consider in the material matrix $\hat{\mathbb{D}}$. Inserting

all interpolations, we introduce the linearized finite element approximation

$$
\begin{aligned}
L\left[G(\boldsymbol{\theta},\delta\boldsymbol{\theta}),\Delta\boldsymbol{\theta}\right] &= \delta\mathbf{v}_e^T \int_{\Omega_e} \left[\, \mathbf{k}_\sigma\, \Delta\mathbf{v} + \mathbf{B}^T\mathbf{N}_\sigma\ \Delta\boldsymbol{\beta} + \mathbf{B}^T\hat{\mathbf{S}} + \mathbf{f}^i - \mathbf{f}^a \,\right] dA \\
&+ \delta\bar{\boldsymbol{\alpha}}^{\boldsymbol{T}} \int_{\Omega_e} \left[\, \bar{\mathbf{N}}_\varepsilon^T\hat{\mathbb{D}}\bar{\mathbf{N}}_\varepsilon\ \bar{\boldsymbol{\alpha}} + \bar{\mathbf{N}}_\varepsilon^T\hat{\mathbb{D}}\bar{\mathbf{N}}_\varepsilon\ \Delta\bar{\boldsymbol{\alpha}} \,\right] dA \\
&- \delta\bar{\boldsymbol{\alpha}}^{\boldsymbol{T}} \int_{\Omega_e} \left[\, \hat{\mathbf{N}}_\varepsilon^T\mathbf{N}_\sigma\,\Delta\boldsymbol{\beta} + \hat{\mathbf{N}}_\varepsilon^T\mathbf{N}_\sigma\,\boldsymbol{\beta} + \mathbf{f}^e \,\right] dA \\
&+ \delta\boldsymbol{\beta}^{\boldsymbol{T}} \int_{\Omega_e} \left[\, \mathbf{N}_\sigma^T\mathbf{B}\ \Delta\mathbf{v} - \mathbf{N}_\sigma^T\hat{\mathbf{N}}_\varepsilon\ \Delta\boldsymbol{\alpha} + \mathbf{N}_\sigma^T\varepsilon_g - \mathbf{N}_\sigma^T\hat{\mathbf{N}}_\varepsilon\boldsymbol{\alpha} + \mathbf{f}^s \,\right] dA \quad .
\end{aligned}
\tag{65}
$$

We simplify the formulation and define the following element matrices

$$
\begin{aligned}
\mathbf{k}_{g[18\times18]} &= \int_{\Omega_e} \mathbf{k}_\sigma\, dA & \mathbf{f}^i_{[18]} &= \int_{\Omega_e} \mathbf{B}^T\hat{\boldsymbol{S}}^h\, dA = \mathbf{G}^T\boldsymbol{\beta} \\
\bar{\mathbf{H}}_{[34\times34]} &= \int_{\Omega_e} \bar{\mathbf{N}}_\varepsilon^T\,\hat{\mathbb{D}}\,\bar{\mathbf{N}}_\varepsilon\, dA & \mathbf{f}^e_{[34]} &= \int_{\Omega_e} \bar{\mathbf{N}}_\varepsilon^T\,\partial_{\boldsymbol{\varepsilon}}W\, dA - \mathbf{F}\,\boldsymbol{\beta} = \begin{bmatrix} \mathbf{f}^e_{1\,[18]} \\ \mathbf{f}^e_{2\,[16]} \end{bmatrix} \\
\mathbf{F}_{[18\times18]} &= \int_{\Omega_e} \hat{\mathbf{N}}_\varepsilon^T\,\mathbf{N}_\sigma\, dA & \mathbf{f}^s_{[18]} &= \int_{\Omega_e} \mathbf{N}_\sigma^T\,\boldsymbol{\varepsilon}_g^h\, dA - \mathbf{F}^T\,\boldsymbol{\alpha} \quad . \\
\mathbf{G}_{[18\times18]} &= \int_{\Omega_e} \mathbf{N}_\sigma^T\,\mathbf{B}\, dA
\end{aligned}
\tag{66}
$$

We solve the integrals in (50) and (66) numerically with a 2×2 Gauss scheme. By means of the element matrices, the linearized variational formulation of equation (65) can be simplified as

$$
\begin{aligned}
L\left[G(\boldsymbol{\theta},\delta\boldsymbol{\theta}),\Delta\boldsymbol{\theta}\right] &= \delta\mathbf{v}_e^T \left[\, \mathbf{k}_g\,\Delta\mathbf{v} + \mathbf{G}^T\ \Delta\boldsymbol{\beta} + \mathbf{f}^i - \mathbf{f}^a \,\right] \\
&+ \delta\bar{\boldsymbol{\alpha}}^{\boldsymbol{T}} \left[\, \bar{\mathbf{H}}\ \Delta\bar{\boldsymbol{\alpha}} \,\right] - \delta\bar{\boldsymbol{\alpha}}^{\boldsymbol{T}} \left[\mathbf{F}\Delta\boldsymbol{\beta} + \mathbf{f}^e\right] \\
&+ \delta\boldsymbol{\beta}^{\boldsymbol{T}} \left[\, \mathbf{G}\ \Delta\mathbf{v} - \mathbf{F}^T\ \Delta\boldsymbol{\alpha} + \mathbf{f}^s \,\right] \quad .
\end{aligned}
\tag{67}
$$

The element matrix $\bar{\mathbf{H}}$ can be partitioned into four submatrices $\mathbf{H}, \mathbf{H}_{mz}, \mathbf{H}_{zm}$, and $\mathbf{H}_{zz}$, thus the thickness components of the shell are separated, as

$$
\begin{aligned}
\bar{\mathbf{H}} &= \int_{\Omega_e} \bar{\mathbf{N}}_\varepsilon^T\hat{\mathbb{D}}\bar{\mathbf{N}}_\varepsilon\, dA = \int_{\Omega_e} \begin{bmatrix} \hat{\mathbf{N}}_\varepsilon & \underline{0} & \underline{0} \\ \underline{0} & \mathbf{N}^z_\varepsilon & \underline{0} \\ \underline{0} & \underline{0} & \tilde{\mathbf{N}}^{el}_\varepsilon \end{bmatrix}^T \mathbb{D} \begin{bmatrix} \hat{\mathbf{N}}_\varepsilon & \underline{0} & \underline{0} \\ \underline{0} & \mathbf{N}^z_\varepsilon & \underline{0} \\ \underline{0} & \underline{0} & \tilde{\mathbf{N}}^{el}_\varepsilon \end{bmatrix} dA \\
&= \begin{bmatrix} \mathbf{H}_{(18\times18)} & \mathbf{H}_{mz(18\times16)} \\ \mathbf{H}_{zm(16\times18)} & \mathbf{H}_{zz(16\times16)} \end{bmatrix}
\end{aligned}
\tag{68}
$$

Including the four matrices into the variational formulation, it follows

$$
\begin{aligned}
L\left[G(\boldsymbol{\theta},\delta\boldsymbol{\theta}),\Delta\boldsymbol{\theta}\right] &= \delta\mathbf{v}_e^T\left[\,\mathbf{k}_g\,\Delta\mathbf{v}+\mathbf{G}^T\,\Delta\boldsymbol{\beta}+\mathbf{f}^i-\mathbf{f}^a\,\right] && (69)\\
&+ \quad \delta\boldsymbol{\alpha}^{\boldsymbol{T}}\left[\,\mathbf{H}\,\Delta\boldsymbol{\alpha}+\mathbf{H}_{mz}\,\Delta\boldsymbol{\alpha}_{\mathbf{33}}^{\boldsymbol{T}}-\mathbf{F}\,\Delta\boldsymbol{\beta}\,+\mathbf{f}^e\right] && (70)\\
&+ \quad \delta\boldsymbol{\alpha}_{\mathbf{33}}\left[\,\mathbf{H}_{zm}\,\Delta\boldsymbol{\alpha}+\mathbf{H}_{zz}\,\Delta\boldsymbol{\alpha}_{\mathbf{33}}\,\right] && (71)\\
&+ \quad \delta\boldsymbol{\beta}^{\boldsymbol{T}}\left[\,\mathbf{G}^T\,\Delta\mathbf{v}-\mathbf{F}^T\,\Delta\boldsymbol{\alpha}+\mathbf{f}^s\,\right] \quad . && (72)
\end{aligned}
$$

Continuity is not required for $\boldsymbol{\alpha}$, $\boldsymbol{\alpha}_{\mathbf{33}}$ and $\boldsymbol{\beta}$ between the elements. Thus, equations (70) - (72) can be set to zero. We solve the system of equations under static condensation of $\Delta\boldsymbol{\alpha}_{33}$ as

$$
\begin{aligned}
&\tilde{\mathbf{H}}\,\Delta\boldsymbol{\alpha}-\mathbf{F}_1\Delta\boldsymbol{\beta}+\bar{\mathbf{f}}^e=\mathbf{0} && \tilde{\mathbf{H}}=\mathbf{H}-\mathbf{H}_{mz}\,\mathbf{H}_{zz}^{-1}\,\mathbf{H}_{zm}\\
&\Delta\boldsymbol{\alpha}_{33}=\mathbf{H}_{zz}^{-1}\left(-\mathbf{f}_2^e-\mathbf{H}_{zm}\,\Delta\boldsymbol{\alpha}\right) && \bar{\mathbf{f}}^e=\mathbf{f}_1^e-\mathbf{H}_{mz}\mathbf{H}_{zz}^{-1}\,\mathbf{f}_2^e \quad .
\end{aligned}
\tag{73}
$$

For $\Delta\boldsymbol{\alpha}$ and $\Delta\boldsymbol{\beta}$ it holds

$$
\begin{aligned}
\Delta\boldsymbol{\alpha} &= \mathbf{F}_1^{-T}\left(\mathbf{G}\,\Delta\mathbf{v}+\mathbf{f}^s\right)\\
\Delta\boldsymbol{\beta} &= \mathbf{F}_1^{-1}\left(\tilde{\mathbf{H}}\,\Delta\boldsymbol{\alpha}+\bar{\mathbf{f}}^e\right) \quad .
\end{aligned}
\tag{74}
$$

Inserting (74) in (69), we obtain the tangential stiffness matrix $\mathbf{k}_T^e$ and the residual vector $\hat{\mathbf{f}}$ on element level. Hence, equation (69) reads

$$
\begin{aligned}
L\left[G(\boldsymbol{\theta}^h,\delta\boldsymbol{\theta}^h),\Delta\boldsymbol{\theta}^h\right] &= \delta\mathbf{v}^T(\mathbf{k}_T^e\,\Delta\mathbf{v}+\hat{\mathbf{f}})=0\\
\mathbf{k}_T^e &= \mathbf{G}^T\,\hat{\mathbf{H}}\,\mathbf{G}+\mathbf{k}_g \qquad\qquad \hat{\mathbf{H}}=\mathbf{F}_1^{-1}\,\tilde{\mathbf{H}}\,\mathbf{F}_1^{-T}\\
\hat{\mathbf{f}} &= \mathbf{G}^T\left(\boldsymbol{\beta}+\hat{\mathbf{H}}\,\mathbf{f}^s+\mathbf{F}_1^{-1}\,\bar{\mathbf{f}}^e\right)-\mathbf{f}^a \quad .
\end{aligned}
\tag{75}
$$

After assembling all elements the problem

$$
\mathbf{K}_T\;\mathbf{V}=\hat{\mathbf{F}} \qquad \text{with} \quad \mathbf{K}_T=\bigcup_{e=1}^{numel}\mathbf{k}_T^e;\;\mathbf{V}=\bigcup_{e=1}^{numel}\mathbf{v}_e;\;\hat{\mathbf{F}}=\bigcup_{e=1}^{numel}\hat{\mathbf{f}}_e \tag{76}
$$

is solved with respect to the nodal degrees of freedom.

6.4 Actuator formulation

In order to deal with the actuator use of piezoelectric shell structures, we postulate a linear distribution of the electric potential in thickness direction. Thus, a value is assigned to the nodal degree of freedom $\Delta\varphi$. We write the corresponding electric field in thickness direction as the average value for every element. According to the gradient relation, see equation (4), the electric potential is divided through the thickness.

$$
\vec{E}_3^e=-\frac{1}{4}\sum_{I=1}^{4}\frac{\Delta\varphi_I}{h} \tag{77}
$$

Hereby, an input variable for the electric field is given and the corresponding parameter of $\boldsymbol{\alpha}_{33}$ is defined. The reduced system of equations according to (69-72) is given as

$$
L=\begin{bmatrix}\delta\mathbf{v}\\ \delta\boldsymbol{\alpha}\\ \delta\boldsymbol{\beta}\end{bmatrix}_e^T\left\{\begin{bmatrix}\mathbf{k}_g & \mathbf{0} & \mathbf{G}^T\\ \mathbf{0} & \mathbf{H} & -\mathbf{F}\\ \mathbf{G} & -\mathbf{F}^T & \mathbf{0}\end{bmatrix}\begin{bmatrix}\Delta\mathbf{v}\\ \Delta\boldsymbol{\alpha}\\ \Delta\boldsymbol{\beta}\end{bmatrix}+\begin{bmatrix}\mathbf{0}\\ \mathbf{H}_{zm}\\ \mathbf{0}\end{bmatrix}\Delta\boldsymbol{\alpha}_{33}+\begin{bmatrix}\mathbf{f}^i-\mathbf{f}^a\\ \mathbf{f}^e\\ \mathbf{f}^s\end{bmatrix}\right\}_e \quad . \tag{78}
$$

7 Numerical examples

7.1 Patchtests

The basic benchmark test of a finite element formulation is the well known patch test. The test is passed if the formulation is able to display a state of constant stresses and constant dielectric displacements along with constant strains and a constant electric field for distributed element geometry. Here, we extend the mechanical patch test according to Reference [53] to the electro-mechanically coupled problem. The geometry of the quadratic patch with distorted elements inside the patch is shown in Figure 5. The material parameters are given as the Young's modulus $E = 67 \cdot 10^3 \frac{MN}{m^2}$, the Poisson's ratio $\nu = 0$, the parameter of the

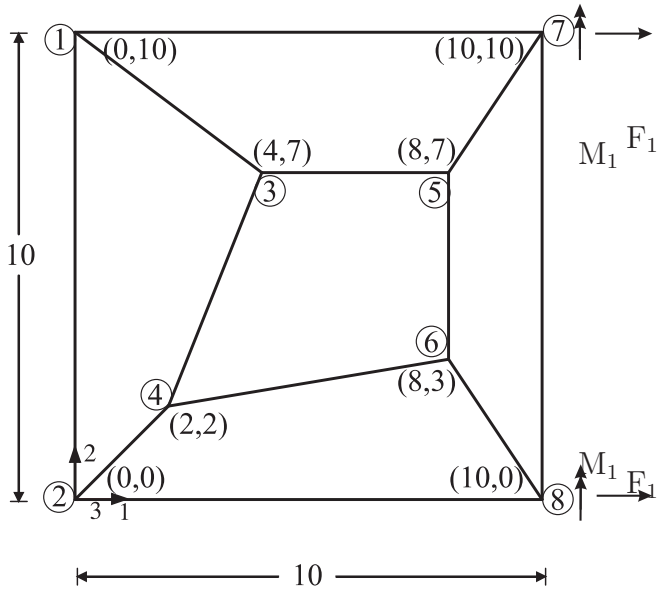

membrane test:
$F_1^{\text{node } 7/8} = 6 \cdot 10^{-2}\text{MN}$
$v_1^{\text{node } 1} = 0,\ v_{1-7}^{\text{node } 2} = 0$

bending test:
$M_1^{\text{node } 7/8} = 1 \cdot 10^{-3}\text{MNm}$
$v_{1-3;\,5-7}^{\text{node } 1/2} = 0$

shear test:
$F_3^{\text{node } 7/8} = 6 \cdot 10^{-2}\text{MN}$
$v_{1-7}^{\text{node } 1/2} = 0,\ v_{1;\,2;\,4-6}^{\text{node } 3-8} = 0$

Figure 5: FE mesh, loading and boundary conditions of the patch test

piezoelectric coupling modulus $e_{13} = 9.3 \frac{C}{m^2}$, $e_{15} = 14.6 \frac{C}{m^2}$ and the dielectric permittivity matrix $\epsilon_{11} = \epsilon_{33} = 15.3 \cdot 10^{-3} \frac{C^2}{MNm^2}$. The thickness is $t = 1m$. For the membrane test we subject nodes seven and eight to the load F_1 in 1-direction. For the bending test, the moment M_1 around the 2-direction is applied on nodes seven and eight. For the shear test the same nodes are subjected to load F_3 in 3-direction. The loadings and the boundary conditions are depicted in Figure 5. The numerical results show that the formulation is able to describe the constant stress states, linear displacement distributions, and the corresponding strain and the electric field states. The numerical results are given in Table 1. The results are compared to the analytical solutions which arise from solving the coupled constitutive equations

$$\begin{aligned} S_{11} &= E\,\varepsilon_{11} - e_{13}\,\vec{E}_3 & \qquad S_{13} &= G\,\gamma_1 \tfrac{5}{6} + e_{15}\,\vec{E}_1 \\ 0 &= e_{13}\,\varepsilon_{11} + \epsilon_{33}\vec{E}_3 & \qquad \vec{D}_1 &= e_{15}\,\gamma_1 + \epsilon_{11}\,\vec{E}_1 \quad . \end{aligned} \tag{79}$$

7.2 Piezoelectric bimorph

The piezoelectric bimorph is a well known piezoelectric benchmark test in order to proof the numerical formulation to the general applicability for sensor and actuator systems. The

Membrane test	$S_{11}[\frac{MN}{m^2}]$	$\vec{E}_3^m[\frac{V}{m}]$	$u_1^{\text{node7/8}}[m]$	
Numerical solution	$1.2 \cdot 10^{-2}$	$-1.004 \cdot 10^{-4}$	$1.652 \cdot 10^{-6}$	
Analytical solution	$1.2 \cdot 10^{-2}$	$-1.004 \cdot 10^{-4}$	$1.652 \cdot 10^{-6}$	
Bending test	$M_{11}[MNm]$	$\vec{E}_3^b[\frac{V}{m}]$	$u_3^{\text{node7/8}}[m]$	$u_5^{\text{node7/8}}[m]$
Numerical solution	$2.0 \cdot 10^{-4}$	$-2.008 \cdot 10^{-5}$	$1.652 \cdot 10^{-6}$	$3.303 \cdot 10^{-7}$
Analytical solution	$2.0 \cdot 10^{-4}$	$-2.008 \cdot 10^{-5}$	$1.652 \cdot 10^{-6}$	$3.303 \cdot 10^{-7}$
Shear test	$Q_{13}[MNm]$	$\vec{E}_1[\frac{V}{m}]$	$u_3^{\text{node7/8}}[m]$	$\Delta\varphi^{\text{node7/8}}$
Numerical solution	$1.2 \cdot 10^{-2}$	$-2.736 \cdot 10^{-4}$	$2.867 \cdot 10^{-6}$	$2.736 \cdot 10^{-3}$
Analytical solution	$1.2 \cdot 10^{-2}$	$-2.736 \cdot 10^{-4}$	$2.867 \cdot 10^{-6}$	$2.736 \cdot 10^{-3}$

Table 1: Numerical and analytical results of the patch tests

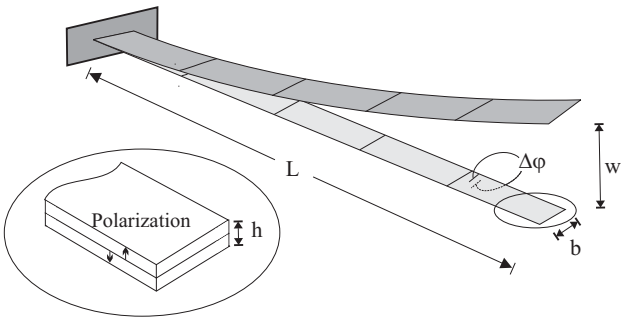

Geometry:

$$\begin{aligned} L &= 0.1m \\ b &= 5 \cdot 10^{-3}m \\ h &= 2 \times 5 \cdot 10^{-4}m \\ w &= 0.01m \end{aligned}$$

Material data:

$$\begin{aligned} E &= 2 \cdot 10^9 \tfrac{N}{m^2} \\ \nu &= 0.29 \\ e_{13} &= -4.6 \cdot 10^{-2} \tfrac{C}{m^2} \\ \epsilon_{33} &= 1.062 \cdot 10^{-10} \tfrac{C^2}{Nm^2} \end{aligned}$$

Figure 6: Geometry and material parameters of the piezoelectric bimorph.

cantilever consists of two piezoelectric PVDF layers poled in opposite direction and was introduced by Tzou and Tseng [58]. Since then, the test has been numerously used, e.g. by Hwang and Park [59] and by Chee et al. [60]. The system is shown in Figure 6. For the discretisation, five elements are chosen, which correspond to five pairs of electrodes that are put along the length of the cantilever. The geometry parameter with the length L, the width b, and the total thickness h as well as the material data are summarized in Figure 6. For the sensor test the bimorph is loaded by a prescribed displacement w. Due to the deflection, an electric potential arises. With the assumption that the potential is measured by means of five pairs of electrodes, we get a staircase function along the length of the cantilever. The results are given in Figure 7(a) and are compared with other piezoelectric finite element formulations from the literature. Whereas [59] also shows a staircase function for a layered plate element and a shallow shell element, [60] and [58] give a linear distribution for a beam element and for a plate/shell element respectively. The linear distribution here results from the disregard of the electrodes and just represents the continuous material curve.

For the actuator test the structure is subjected to an electric potential $\Delta\varphi = 5 \cdot 10^{-4}\ V$ that brings about an electric field $\vec{E} = 1\frac{V}{m}$. Due to the opposite polarization of the layers the upper layer shortens and the lower layer elongates. The resultant deflection is depicted in Figure 7(b). The bimorph has a tip deflection of $w = 3.45\mu m$, which corresponds to the solution of an analytical calculation with a Bernoulli beam, see Tzou [61].

In order to analyze the influence of mesh distortion, the finite element mesh of the bimorph

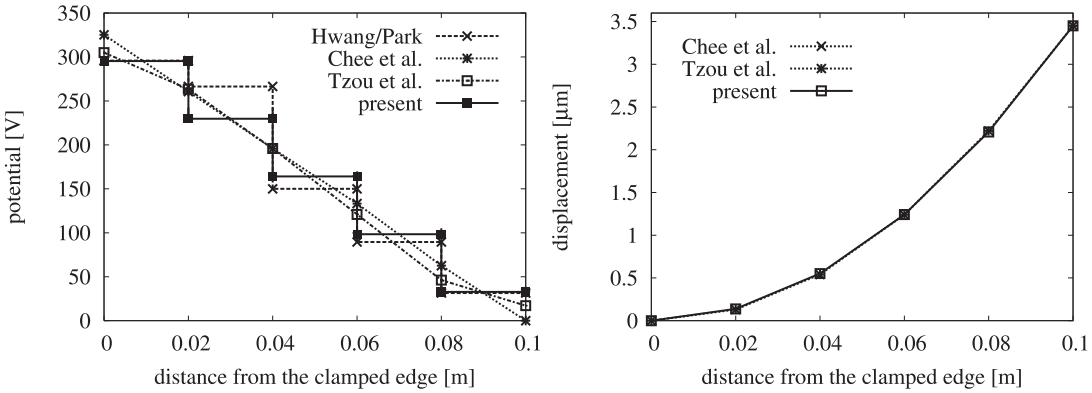

Figure 7: Distribution of the electric potential along the bimorph structure for sensor usage (a) and deflection of the bimorph due to actuator loading (b).

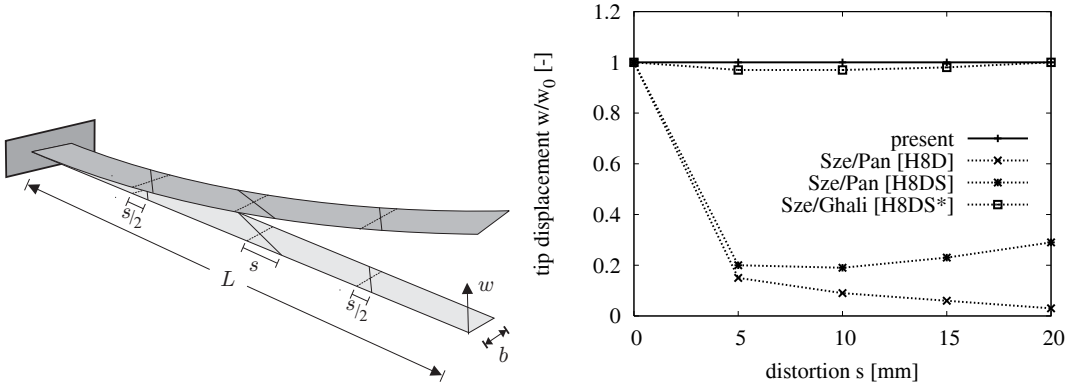

Figure 8: System and resluts for the bimorph with distorted mesh.

is modified according to Sze und Pan [62]. The initial configuration has four rectangular elements. Then the nodes become disarranged by the parameter s, see Figure 8. The bimorph is subjected to an electrical field $1\frac{V}{m}$ again. The tip deflection, normalized on the analytical solution $w_0 = 3.45\mu m$, is depicted in Figure 8, dependent on the distortion parameter s. We compare the results with the data given by Sze and Pan [62] and by Sze and Ghali [63] for the mixed hexahedral elements (H8D and H8DS) and (H8DS*), respectively. Here the elements "H8D" and "H8DS" vary in the number of independent variables. The element "H8D" has independent variables for the displacement, the electric potential and the dielectric displacements, in "H8DS" also the stresses are included. But the results can hardly be improved. Good results are obtained by the element "H8DS*" of Sze and Ghali [63], which decreases the impact of shear locking effect by selective scaling technique. The present shell element does not show any shear locking, thus the results fit the analytical solution even for strong distorted meshes.

Geometry	PZT ceramic
$R = 0.2m$	$E_1 = E_2 = 81.3.0 \cdot 10^9 \frac{N}{m^2}$
$b = 0.2m$	$E_3 = 64.5 \cdot 10^9 \frac{N}{m^2}$
$h = 2 \cdot 10^{-3}m$	$G_{12} = 30.6 \cdot 10^9 \frac{N}{m^2}$
$h_{PZT} = 0.5 \cdot 10^{-3}m$	$G_{23} = 25.6 \cdot 10^9 \frac{N}{m^2}$
$h_{GraphitEpoxid} = 4 \times 0.375 \cdot 10^{-3}m$	$\nu_{12} = 0.33$
Graphite Epoxy	$\nu_{13} = \nu_{23} = 0.43$
$E_1 = 132.4 \cdot 10^9 \frac{N}{m^2}$	$e_{13} = -14.8 \frac{C}{m^2}$
$E_2 = E_3 = 10.8 \cdot 10^9 \frac{N}{m^2}$	$e_{15} = 12.67 \frac{C}{m^2}$
$G_{12} = G_{13} = 5.6 \cdot 10^9 \frac{N}{m^2}$	$\epsilon_{11} = 13.054 \cdot 10^{-9} \frac{C^2}{Nm^2}$
$G_{23} = 3.6 \cdot 10^9 \frac{N}{m^2}$	$\epsilon_{33} = 11.505 \cdot 10^{-9} \frac{C^2}{Nm^2}$
$\nu_{12} = \nu_{21} = 0.24$; $\nu_{23} = 0.49$	

Table 2: Geometry and material parameters for the 90° cylindrical shell.

7.3 90° cylindrical shell

We choose a 90° cylindrical shell in order to analyze layered shell structures. The system, see Figure 9, consists of four graphite epoxy layers, for which we account the orientation angles φ_F with [0/90/90/0] referring to the x axis. The lower surface is bordered by a piezoelectric PZT layer. The geometry and the material parameters for the graphite epoxy

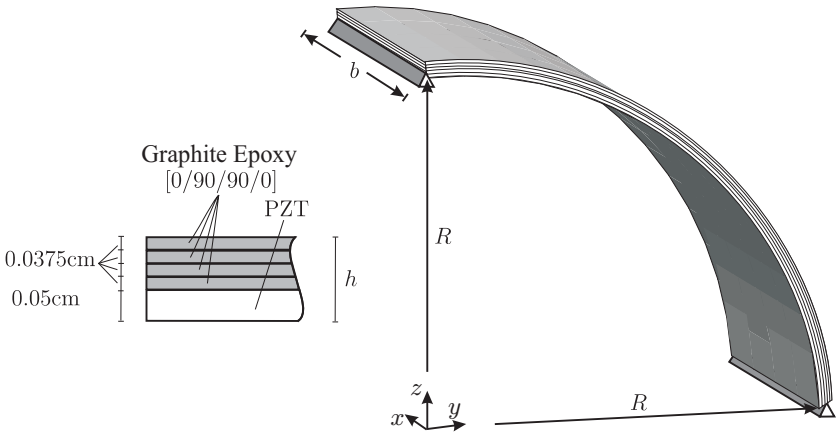

Figure 9: Layered 90° cylindrical shell.

and PZT layers according to Balamurugan and Narayanan [64] are given in Table 2. The system is simply supported at the rectilinear edges and is modeled by 15×4 elements with 15 elements in circumference direction and 4 elements for the width b. The ratio of the radius R of the middle surface to the thickness h is given by $R/h = 100$. The piezoelectric layer works as actuator and is subjected to an electric field of $\vec{E} = -400V/mm$. The radial system displacement w is measured along the centerline at $b/2$. The results, normalized by the thickness h, are depicted in Figure 10 dependent on the normalized radius R between 0° and 90° of the cylinder segment. We compare the present shell formulation with data from Balamurugan and Narayanan [64] for a degenerated nine-node quadrilateral shell element with

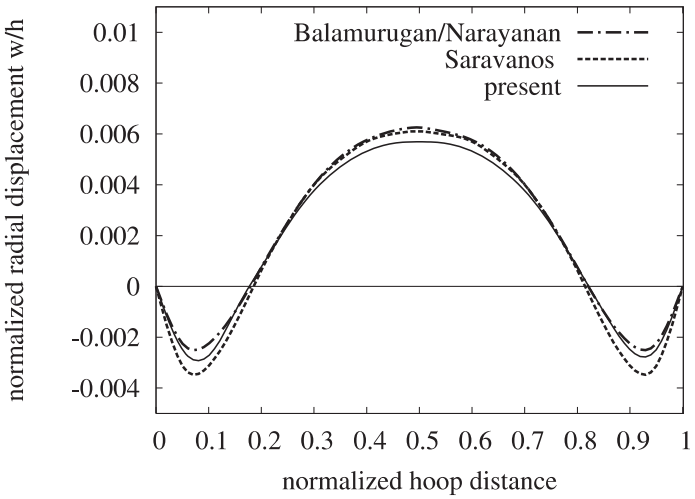

Figure 10: Normalized radial displacement of the 90° cylindrical shell at $x = b/2$.

quadratic approach for the electric potential in thickness direction and with Saravanos [65] who provides a laminated eight-node shell element with lineare electric thickness potential. The good accordance of the results shows the reliable applicability of the present laminated four node formulation for layered piezo-mechanical structures.

7.4 Steering of an antenna

In this example, we show two versions of an antenna that can be manipulated via piezoelectric devices. We analyze both a spherical antenna with two piezoelectric patches at the lower surface according to experimental studies by Gupta et al. [66, 67] and a parabolic antenna

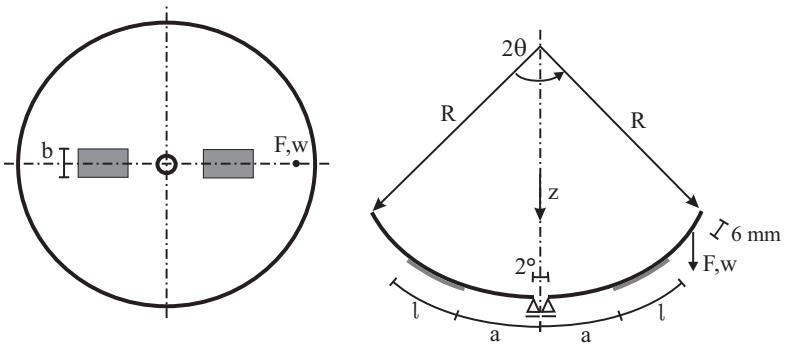

Figure 11: Geometry of the antenna.

with four isochronously arranged piezoelectric segments. First, we consider an aluminium antenna as part of a spherical shell, see Figure 11, with a radius R and an aperture angle 2θ. Two piezoelectric patches with the width b and the length l are arranged with the distance a from the small hole of 2° in the middle of the antenna shell. The geometry and material data are summarized in Table 3. We completed missing material parameters, marked by $()^*$, with empirical data of similar material behavior. For the finite element model the rectangular

Geometry	Piezo patches	Aluminium shell
$R = 0.203m$	$E = 66.0 \cdot 10^9 \frac{N}{m^2}$	$E = 53.0 \cdot 10^9 \frac{N}{m^2}$
$\theta = 45$	$\nu = 0.178$	$\nu = 0.3$
$a = 0.05m$	$e_{13} = -5.6 \frac{C}{m^2}$	
$t_{shell} = 0.36 \cdot 10^{-3}m$	$e_{33} = 17.3 \frac{C}{m^2}$	
$t_{patch} = 0.267 \cdot 10^{-3}m$	$e^*_{15} = 13.0 \frac{C}{m^2}$	
$b = 23.8 \cdot 10^{-3}m$	$\epsilon^*_{11} = \epsilon^*_{33} = 1.53 \cdot 10^{-8} \frac{C^2}{Nm^2}$	
$l = 36.0 \cdot 10^{-3}m$		

Table 3: Geometry and material parameter of the antenna with piezoelectric patches.

piezoelectric patches are adapted to the finite element mesh. For this we retain the area of the patches unchanged and the center of gravity stay the same for both the initial and the adjusted trapezoidal geometry of the patches. The width of the patches is characterized by an angle of 22.5°. The patches range from 13.375° from the center point of the antenna to 25.0625°. For the boundary conditions we assume that the displacement in z-direction at the nodes of the inner hole are fixed. With respect to the symmetric system, we model only half of the structure by 32x64 elements.

Case I: Mechanical loading

We subject the antenna in z-direction to a point load F, which affects the antenna in the symmetry plane through the piezo patches $6mm$ under the top edge. The resultant displacement w of the loading point in z-direction is presented in Table 4. We compare those results to the experimental data and a numerical calculation with a reduced eight-node element by Gupta et al. [67].

Load F [N]	Experiment [mm]	Gupta [mm]	present [mm]
0.02	0.194	0.1852	0.191
0.05	0.475	0.4630	0.477
0.07	0.663	0.6482	0.668
0.1	0.959	0.9260	0.954
0.12	1.165	1.1112	1.145
0.15	1.466	1.3890	1.431

Table 4: Displacement w of the antenna due to the load F.

Case II: Symmetric actuator loading

In order to manipulate the range of the antenna, we connect a voltage to the patches. As a result from the electric loading, a deflection occurs. The load-deflection curve is shown in Figure 12(a) for an electric potential of 0 to 100 Volt, which is simultaneously connected to both patches. The resultant displacement w is measured as in case I in the symmetry plane $6mm$ under the top edge. As depicted in Figure 12(a), the numerical results and the experimental data are close together.

Fall III: Asymmetric actuator loading

To change the range asymmetrically, the patches are subjected to different electric voltages. Therefore, one patch is subjected to $150V$ and the other patch to $75V$. We measure the

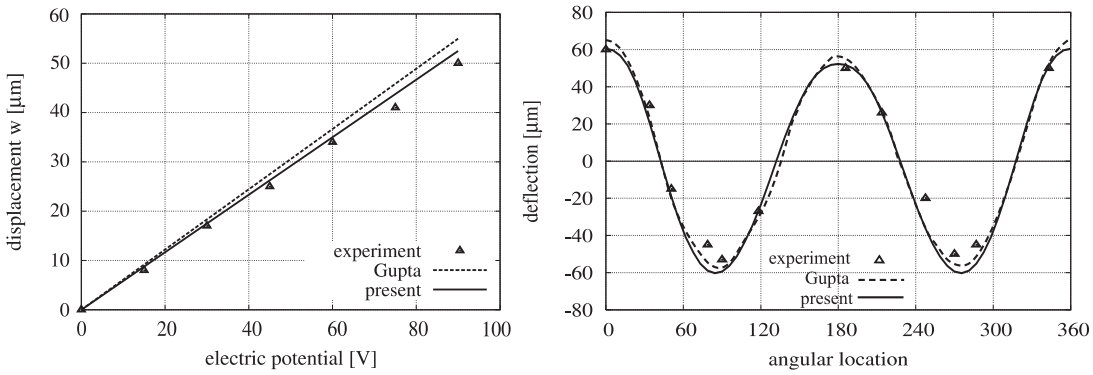

Figure 12: Electric potential - displacement curve of the antenna for the actuator usage under symmetrical loading (a) and deflection for actuator usage under asymmetric loading [150V/75V](b).

deformation of the antenna in z-direction around the circumference $6mm$ under the top edge. Figure 12(b) shows the displacement curve dependent on the angle around the middle axis of the antenna.

Parabolic antenna with piezoelectric segments

To enlarge the total displacements of the antenna Gupta [66] provides a parabolic antenna geometry with four piezoelectric actuator segments isochronously attached at the lower surface, see Figure 13. The shell with the thickness $t = 0.203mm$ has an elastic modulus $E = 20{\cdot}10^9 \frac{N}{m^2}$

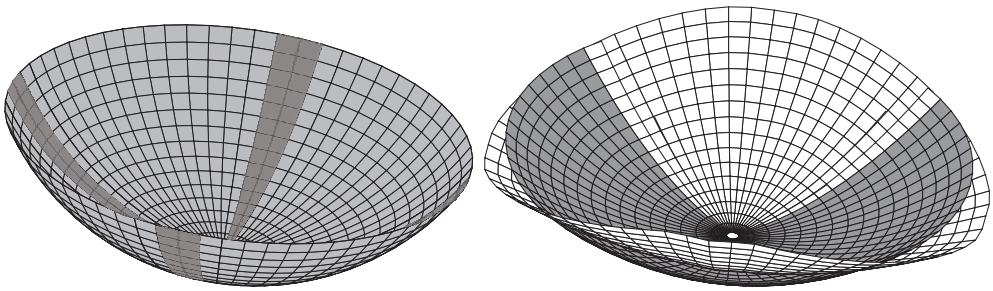

Figure 13: Parabolic antenna with piezoelectric segments (a); Parabolic antenna in original state and deformed system according to loading case 2 (b).

and a Poisson's ratio $\nu = 0.3$. The material data for the piezoelectric actuators correspond to the parameters given in Table 3. The segments have an angle of 11.25° each. The geometry is shown in Figure 14 as top view and as cut through the symmetry plane at AC. The geometry of the antenna shell is characterized by the equation $z = \frac{7.5}{17.5^2}(x^2 + y^2) - 7.5$. We model the antenna with 64 elements in circumferential direction and 16 elements from the inner hole to the top edge. According to the anchorage of the antenna by means of a screw in the middle of the antenna shell, the displacement degrees of freedom at the inner hole are fixed. Additionally, the rotation around the local z-axis at the hole and at the top edge is fixed. The piezoelectric material is poled in thickness direction and is attached to the structure in a way, that the polarization direction is set from outside to the inside of the shell. In order to change the range of the antenna, we impress a voltage on the piezoelectric segments. Here,

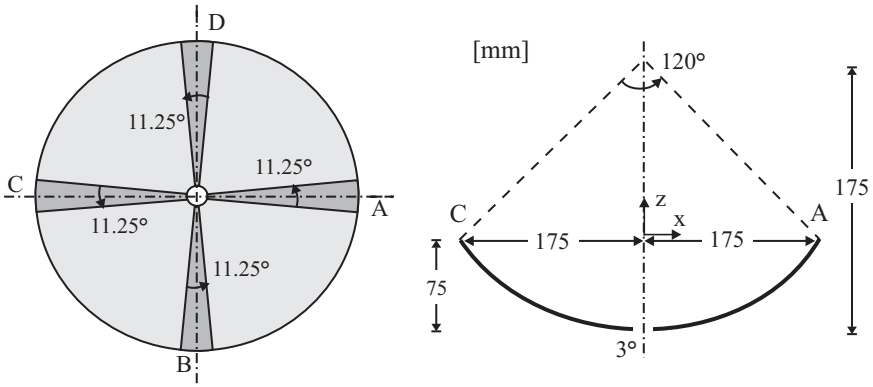

Figure 14: Geometry of the parabolic antenna.

we distinguish between the following loading cases

1. $\Delta\varphi = +300V$ for all actuator segments

2. $\Delta\varphi = +300V$ for the actuator segments at A and C
   $\Delta\varphi = -300V$ for the actuator segments at B and D

3. $\Delta\varphi = +300V$ for the actuator segments at A and B
   $\Delta\varphi = -300V$ for the actuator segments at C and D

The deformed system for the loading case 2 is depicted in Figure 13 (scaled by the factor 10). The subfigures of 15 show the original state of the antenna and the deformed structure along the axis AC and BD, respectively. For an easier evaluation of the deformation, we introduce appropriate scaling factors, see Figure 15. For the loading case 1, the antenna completely expands, whereas the total displacements are small. Thus, the whole range of the antenna can be extended. The displacement in z-direction for the points A,B,C, and D is $0.715mm$. The loading case 2 enlarges the range in one axis and diminishes it perpendicular to this axis. Here the displacement at the points A and C holds $-4.860mm$ and at the points B and D $+4.860mm$. A rotation of the antenna to the left hand side can be reached by the loading of case 3. The displacement in z-direction of A and B counts $-1.359mm$ and for C and D $+1.359mm$. The result given by [66] for case 1 is a displacement of $0.7mm$, for case 2 $\pm 7.0mm$ and for case 3 $\pm 1.3mm$.
The results of the loading cases 1 and 3 correspond very well to the data from the literature. In case 2 there are deviations. This is potentially caused by the complex geometry or in the differences of the formulation. The results in [66] correspond to a selective reduced eight node element.

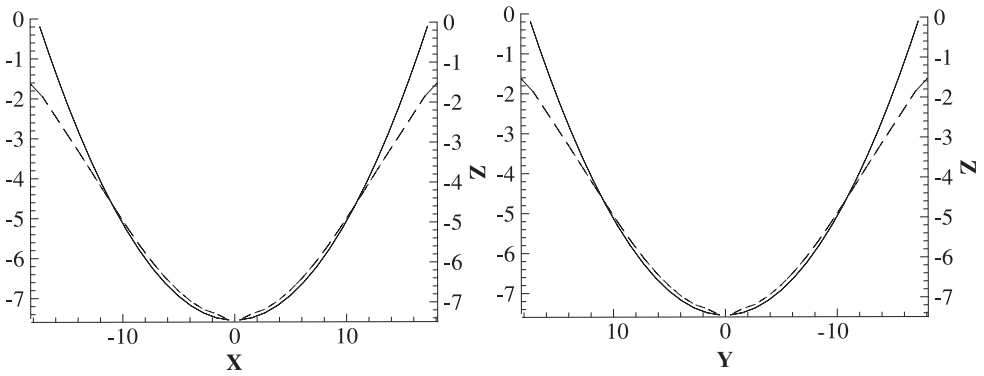

(a) Loading case 1 (A=B=C=D=300V), scaling factor 20; $\mathbf{x} = \mathbf{X} + 20\mathbf{u}$.

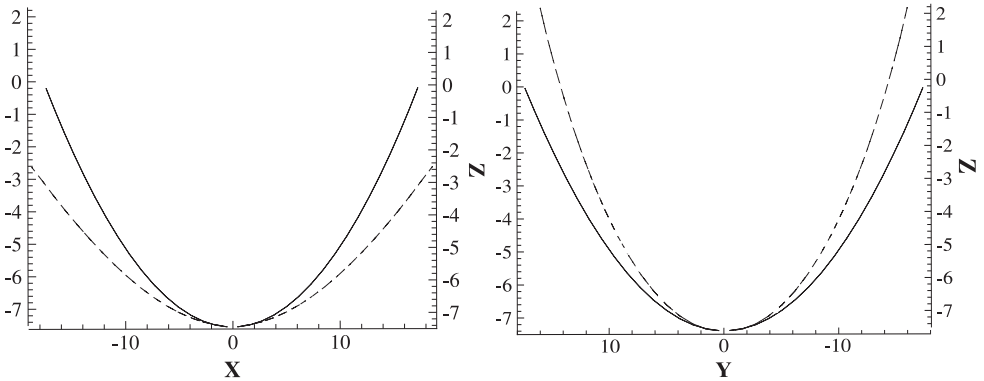

(b) Loading case 2 (A=C=300V, B=D=-300V) , scaling factor 5; $\mathbf{x} = \mathbf{X} + 5\mathbf{u}$.

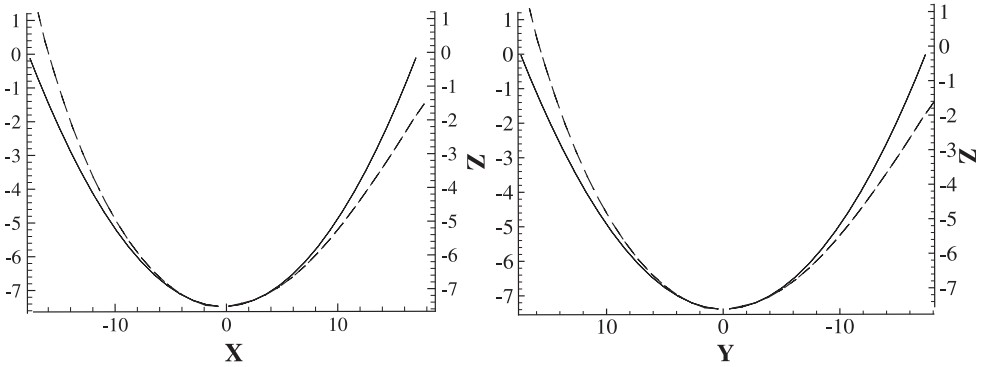

(c) Loading case 3 (A=B=300V, C=D=-300V) , scaling factor 10; $\mathbf{x} = \mathbf{X} + 10\mathbf{u}$.

Figure 15: Deformation of the parabolic antenna for the loading cases 1, 2 and 3 along the axis AC and BD. (——— original state, – – – deformed state)

7.5 Test of the Preisach model for ferroelectric hysteresis

In order to validate the results of the temperature-dependent Preisach model for the ferro-

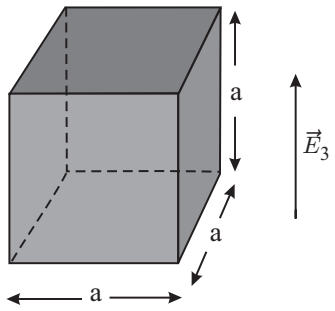

Material data	Preisach parameter
$E = 6.0 \cdot 10^9 \frac{N}{m^2}$	$c = 100/\pi$
$\nu = 0.34$	$f_\alpha = 50$
$e_{13} = -6.55 \frac{C}{m^2}$	$f_\beta = 50$
$e_{33} = 23.3 \frac{C}{m^2}$	$y_\alpha = 0.5$
$e_{15} = 0.0 \frac{C}{m^2}$	$y_\beta = -0.5$
$\varepsilon_{11} = 2.77 \cdot 10^{-8} \frac{C^2}{Nm^2}$	Geometry
$\varepsilon_{33} = 3.01 \cdot 10^{-8} \frac{C^2}{Nm^2}$	$a = 0.001m$
$\vec{E}_c = 0.6 \cdot 10^6 \frac{V}{m}$	
$\vec{P}_{sat} = 0.33 \frac{C}{m^2}$	
$E_{sat} = 0.002$	

Figure 16: Geometry, material and Preisach parameter for the test specimen.

electric hysteresis effects, a simple material cube made of soft PZT with an edge length a, see Figure 16, is chosen. This test specimen was introduced by Mauck and Lynch [36], to depict the dielectric and the butterfly hysteresis for different temperatures. In [36], experimental results are given for the polarization and the expansion behavior under an electric field tested at the temperatures 25°C (298K) and 100°C (373K). Besides experimental results also a micro-mechanical model is introduced in [36]. The formulation is based on the principles of energy conservation and models the nonlinear behavior of polycrystal ferroelectric materials

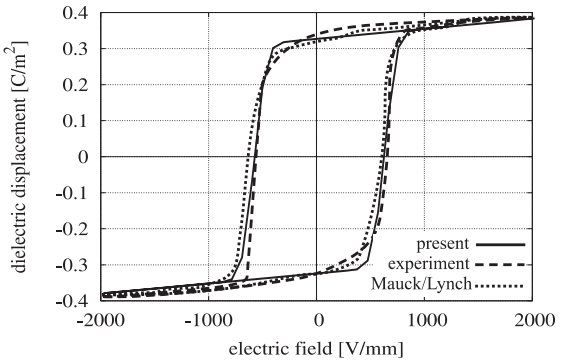

(a) Dielectric hysteresis for 25°C.

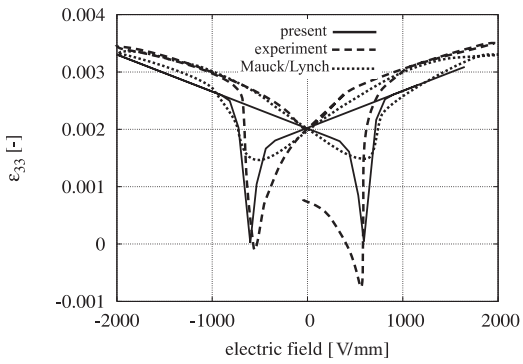

(b) Butterfly hysteresis for 25°C.

Figure 17: Hysteresis curves for 25°C

with a switching criterion that accounts for temperature effects. For the micro-mechanical calculation, the material paramters in [36] are derived from the single crystal parameters of barium titanate and are modified via a correction parameter to get the material parameter of soft PZT single crystal. According to Reference [26], we choose the macroscopic material parameter for soft PZT polychristals as given in Figure 16. We compare the numerical results of the present formulation with the experimental data and the micromechanical model in [36]. Figure 17 presents the dielectric hysteresis and the butterfly hysteresis for a temperature of

25°C. Figure 17(a) shows that the dielectric hysteresis curve at 25°C can be described very well. For the strain hysteresis in 17(b) the reversible strains are slightly underestimated. However, the present formulation is not able to display the nonlinear reversible part but assumes linear distributions. Whereas the micromechanical model does not reach the strain peaks in the butterfly hysteresis, this can be managed well by means of the presented Preisach model. Figure 18 depicts the hysteresis curves for a temperature of 100°C. The dielectric hysteresis

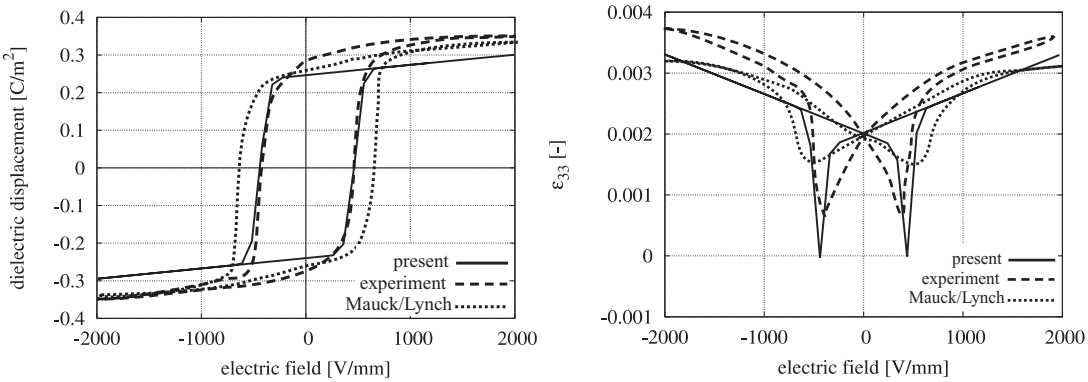

(a) Dielectric hysteresis for 100°C.

(b) Butterfly hysteresis for 100°C.

Figure 18: Hysteresis curves for 100°C

in Figure 18(a) shows the good accordance of the present formulation with the experimental results in the region of the electric coercitive field. However above the saturation values the reversible part is underestimated. Here, the micro-mechanical model of Reference [36] achieves better solutions. But for 100°C it gets higher coercitive values, thus the hysteresis area and thus the switching energy is overestimated. The differences in the reversible variables can also be detected in the butterfly hysteresis in Figure 18(b). Analyzing Figure 18(b), one can see that the hysteresis peaks are smaller in the experiment as in the numerical model. Thus we conclude that also the saturation strains must change with temperature and become smaller in this case. Due to a lack of sufficient experimental data in the literature for this aspect we derive a linear relationship for the saturation strain, $E_{sat} = -9.333 \cdot 10^{-3} T[Kelvin] + 4.7813$, from the two depicted curves for 25°C and 100°C as first simplified approximation. Though this assumption has to be verified by further experimental investigations. The model of Mauck and Lynch can not display the peaks correctly. Furthermore they obtain the minima for absolut values of the electric field which are too high.

7.6 Piezoelectric ceramic disc

A thin piezoelectric PZT ceramic disc is introduced by Yimnirun et al. [38] who gives experimental results for the temperature-dependent polarization behavior, see Figure 19. The disc with an outer diameter d_1 and the thickness t is subjected to an electric field in thickness direction for different temperatures in the range of 298 to 453 Kelvin. For the numerical calculation we choose the three representative temperatures $298K$, $373K$ and $453K$. To simplify the calculation, we additionally introduce a small hole at the disc center characterized by the diameter d_2, which lets the polarization change unaffected and thus does not influence the

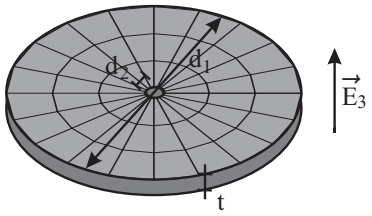

Material parameter	Preisach parameter
$E = 5.9 \cdot 10^9 \frac{N}{m^2}$	$c = 25/\pi$
$\nu = 0.34$	$f_\alpha = 12.5$
$e_{13} = -6.55 \frac{C}{m^2}$	$f_\beta = 12.5$
$e_{33} = 23.3 \frac{C}{m^2}$	$y_\alpha = 0.5$
$e_{15} = 17.0 \frac{C}{m^2}$	$y_\beta = -0.5$
$\epsilon_{11} = 1.5 \cdot 10^{-8} \frac{C^2}{Nm^2}$	Geometry
$\epsilon_{33} = 1.5 \cdot 10^{-8} \frac{C^2}{Nm^2}$	$d_1 = 8 \cdot 10^{-3} m$
$\vec{E}_c = 1.05 \cdot 10^6 \frac{V}{m}$	$d_2 = 0.5 \cdot 10^{-3} m$
$\vec{P}_{sat} = 0.34 \frac{C}{m^2}$	$t = 1 \cdot 10^{-3} m$
$E_{sat} = 0.002$	

Figure 19: Geometry, material and Preisach parameter for the piezoelectric ceramic disc.

dielectric hysteresis curve. The geometry, the material parameters, and the Preisach parameters are summarized in Figure 19. The missing parameters of the permittivity are added from experienced data. Figure 20 shows the polarization behavior of the disc for $298K$, $373K$ and $453K$, respectively. With increasing temperature, the hysteresis curve becomes more compact and the hysteresis area decreases. The coercitive electric field and the saturation polarization are the same as in the experimental investigation of Yimnirun et al. [38], thus the switching

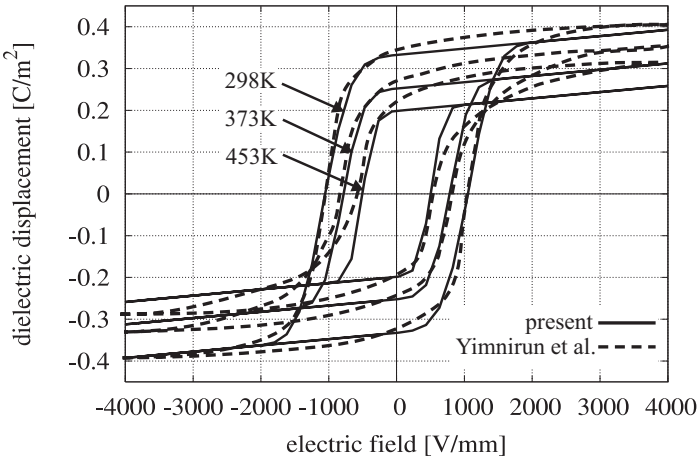

Figure 20: Temperature dependent dielectric hysteresis.

processes can be displayed very well. However, the reversible polarization is underestimated compared to the experiment and shows a nonlinear behavior. Due to the complex relation this is not incorporated in the present model. For an exact description of the hysteresis curves this has to be analyzed in further research.

7.7 Telescopic cylinder

The quite small displacements of piezoelectric structures can be enlarged by special architectures. With several nested cylinders, which are alternately connected at the top and the bottom, actuators with much higher displacements and be composed. Alexander et al. [69]

Geometry	Material parameter	Preisach parameter
$h = 2.375 \cdot 10^{-2} m$	$E = 60.6 \cdot 10^9 \frac{N}{m^2}$	$c = 25/\pi$
$t = 0.1 \cdot 10^{-2} m$	$\nu = 0.4$	$f_\alpha = 12.5$
$r1 = 0.275 \cdot 10^{-2} m$	$e_{13} = -29.88 \frac{C}{m^2}$	$f_\beta = 12.5$
$r2 = 0.425 \cdot 10^{-2} m$	$e_{33} = 10.64 \frac{C}{m^2}$	$y_\alpha = 0.5$
$r3 = 0.575 \cdot 10^{-2} m$	$e_{15} = 27.26 \frac{C}{m^2}$	$y_\beta = -0.5$
$r4 = 0.725 \cdot 10^{-2} m$	$\epsilon_{11} = \epsilon_{33} = 1.0693 \cdot 10^{-8} \frac{C^2}{Nm^2}$	
$r5 = 0.875 \cdot 10^{-2} m$	$\vec{E}_c = 0.8 \cdot 10^6 \frac{V}{m}$	
	$\vec{P}_{sat} = 0.49 \frac{C}{m^2}$	
	$E_{sat} = 0.002$	

Table 5: Geometry, material and Preisach parameter of the telescopic actuator.

introduce a telescopic actuator made of five cylinders, see Figure 21. It has a height of $25mm$

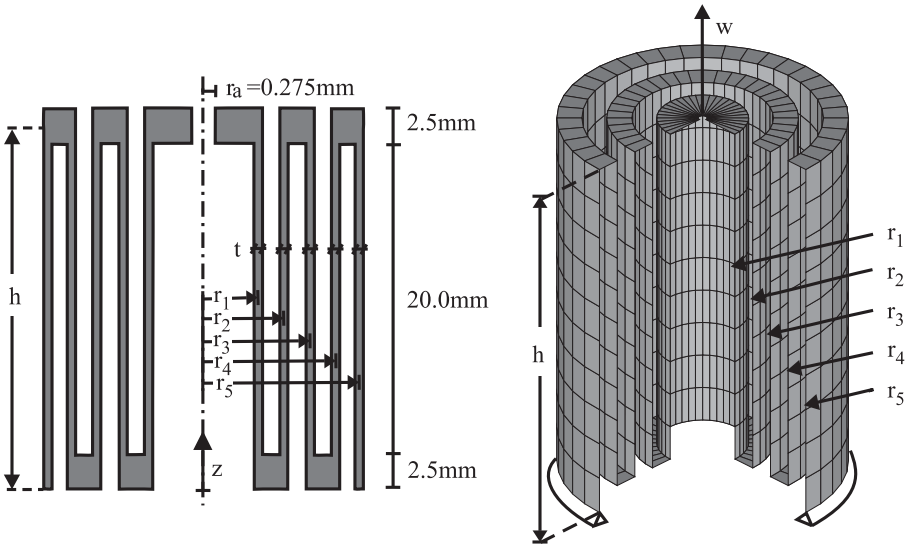

Figure 21: Geometry and finite element discretization of the telescopic cylinder.

and an outer diameter of $18.5mm$. The five cylinders have a thickness of $t = 1mm$ each and are alternately connected at the top and the bottom by a connective element with a thickness of $2.5mm$. At the top, the inner cylinder is closed by a $2.5mm$ thick plate with a small hole in the center holding the radius $r_a = 0.275mm$. The radii of the cylinders numerated from the inner to the outer tube are r_1, r_2, r_3, r_4 and r_5 and correspond to the middle surface of every cylinder. The finite element discretization is shown in Figure 21. However, with respect to the symmetry for the numerical calculation, only a quarter of the system with the corresponding symmetry boundary conditions is modeled. The geometry, the material data, and the Preisach parameters for the material nonlinear calculation are summarized in Table 5. The cylinders are subjected to an electric potential in radial direction in such a way that the cylinders alternately expand and shorten. The displacements at the lower edge of the outer cylinder are fixed, thus the maximal displacement in z-direction w is measured at the hole in

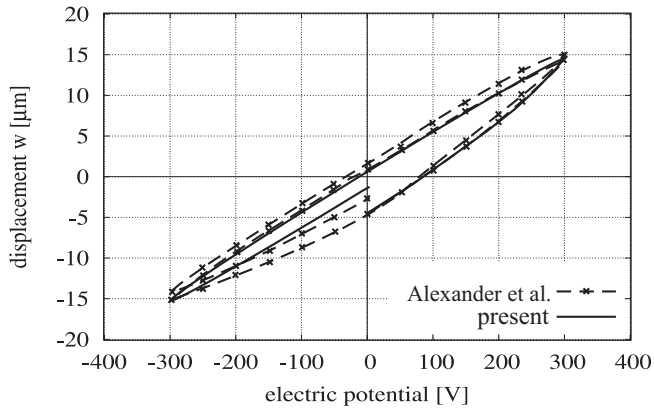

Figure 22: potential-displacement curve of the telescopic cylinder for actuator usage.

the middle of the top plate at the inner cylinder. In order to compare the numerical results with the experimental data of Reference [69], an electric potential of $-1200V$ is connected to the structure, thus the material is fully poled. Afterwards, we run the load circle $0V$, $300V$, $-300V$, $0V$. With respect to the material nonlinear behavior, it results a hysteresis curve for the maximal displacement w, which is displayed in Figure 22 together with the experimental data from [69]. The good accordance of the remanent displacement due to the initial loading by $-1200V$, read off for an electric potential of $0V$, with the experiment and the well representable subhysteresis for $\pm 300V$ show the applicability of the introduced finite shell formulation for the presented system. An open question is how the experimental results reach the initial value of the remanent displacement again after $-1200V$ for the first subhysteresis $\pm 300V$. In [69] it seems that not until the second subcycle the estimated smaller displacement is obtained, which does not accord with the description in Reference [29]. The numerical results are almost identical to the analysis of [70], that is based on a continuum element with an energy switching model.

8 Conclusions

In this paper, we have presented a piezoelectric finite shell element. The mixed hybrid formulation includes independent thickness strains, which allows a consideration of three-dimensional nonlinear constitutive equations. By means of a temperature-dependent Preisach model we consider the actual polarization state and thus we incorporate ferroelectric hysteresis phenomena. With only one electrical degree of freedom, the formulation simulates the behavior of both piezoelectric sensor and actuator systems appropriately. The presented examples show the influence of the temperature for the ferroelectric nonlinear behavior.

References

[1] Klinkel S, Wagner W. A piezoelectric solid shell element based on a mixed variational formulation for geometrically linear and nonlinear applications. *Computers and Structures* 2008; **86**:38–46.

[2] Zheng S, Wang X, Chen W. The formulation of a refined hybrid enhanced assumed strain solid shell element and its application to model smart structures containing distributed piezoelectric sensors/actuators. *Smart Materials and Structures* 2004; **13**:N43–50.

[3] Sze K, Yao L, Yi S. A hybrid stress ANS solid-shell element and its generalization for smart structrue modelling part I + II. *International Journal for Numerical Methods in Engineering* 2000; **48**:545–582.

[4] Heyliger P, Pei KC, Saravanos DA. Layerwise mechanics and finite element model for laminated piezoelectric shells. *AIAA Journal* 1996; **34**(11):2353–2360.

[5] Varelis D, Saravanos DA. Coupled mechanics and finite element for non-linear laminated piezoelectric shallow shells undergoing large displacements and rotations. *International Journal for Numerical Methods in Engineering* 2006; **66**(8):1211–1233.

[6] Varelis D, Saravanos DA. Nonlinear coupled multi-field mechanics and finite element for active multi-stable thermal piezoelectric shells. *International Journal for Numerical Methods in Engineering* 2008; **76**:84–107.

[7] Kögel M, Bucalem ML. Locking-free piezoelectric MITC shell elements. In *Computational Fluid and Solid Mechanics,* Bathe KJ (ed). 2003; 392–395.

[8] Bernadou M, Haenel C. Modelization and numerical approximation of piezoelectric thin shells Part I + II + III. *Computer Methods in Applied Mechanics and Engineering* 2003; **192**:4003–4107.

[9] Lammering R, Mesecke-Rischmann S. Multi-field variational formulations and related finite elements for piezoelectric shells. *Smart Materials and Structures* 2003; **12**:904–913.

[10] Lentzen S, Klosowski P, Schmidt R. Geometrically nonlinear finite element simulation of smart piezolaminated plates and shells. *Smart Materials and Structures* 2007; **16**:2265–2274.

[11] Wang X, Wang y. On nonlinear behavior of spherical shallow shells bonded with piezoelectric actuators by the differential quadrature element method (DQEM). *International Journal for Numerical Methods in Engineering* 2002; **53**:1477–1490.

[12] Tan X, Vu-Quoc L. Optimal solid shell element for large deformable composite structures with piezoelectric layers and active vibration control. *International Journal for Numerical Methods in Engineering* 2005; **64**:1981–2013.

[13] Zhou Y, Tzou H. Active control of nonlinear piezoelectric circular shallow spherical shells. *International Journal of Solids and Structures* 2000; **37**:1663–1677.

[14] Tzou H, Bao Y. Nonlinear piezothermoelasticity and multi-field actuations part 2: control of nonlinear deflection, buckling and dynamics. *Journal of Vibration and Acoustics* 1997; **119**:382–389.

[15] Benjeddou A, Deü JF, Letombe S. Free vibrations of simply-supported piezoelectric adaptive plates: An exact sandwich formulation. *Thin-Walled Structures* 2002; **40**:573–593.

[16] Balamurugan V, Narayanan S. A piezolaminated composite degenerated shell finite element for active control of structures with distributes piezosensors and actuators. *Smart Materials and Structures* 2008; **17(3)**:035031.

[17] Miranda S, Ubertini F. Consistency and recovery in electroelasticity part I: Standard finite elements. *Computer Methods in Applied Mechanics and Engineering* 2003; **192**:831–850.

[18] Miranda S, Ubertini F. Consistency and recovery in electroelasticity part II: Equilibrium and mixed finite elements. *Computer Methods in Applied Mechanics and Engineering* 2004; **193**:2155–2168.

[19] Sze KY, Pan YS. Hybrid finite element models for piezoelectric materials. *Journal of Sound and Vibration* 1999; **226**:519–547.

[20] Chen W, Lynch CS. A micro-electro-mechanical model for polarization switching of ferroelectric materials. *Acta Metallurgica* 1998; **46(15)**:5303–5311.

[21] Huber JE, Fleck NA, Landis CM, McMeeking RM. A constitutive model for ferroelectric polycrystals. *Journal of Mechanics and Physics of Solids* 1999; **47**:1663–1697.

[22] Bassiouny E, Ghaleb AF, Maugin GA. Thermodynamical formulation for coupled electromechanical hysteresis effects - I+II. *International Journal of Engineering Science* 1988; **26(12)**:1279–1306.

[23] Bassiouny E, Maugin GA. Thermodynamical formulation for coupled electromechanical hysteresis effects - III. parameter identification. *International Journal of Engineering Science* 1989; **27(8)**:975–987.

[24] Bassiouny E, Ghaleb AF, Maugin GA. Thermodynamical formulation for coupled electromechanical hysteresis effects - IV. combined electromechanical loading. *International Journal of Engineering Science* 1989; **27(8)**:989–1000.

[25] McMeeking RM, Landis CM. A phenomenological multiaxial constitutive law for switching in polycrystalline ferroelectric ceramics. *International Journal of Engineering Science* 2002; **40**:1553–1577.

[26] Kamlah M. Ferroelectric and ferroelastic piezoceramics - modeling of electromechanical hysteresis phenomena. *Continuum Mechanics and Thermodynamics* 2001; **13**:219–268.

[27] Klinkel S. A phenomenological constitutive model for ferroelastic and ferroelectric hysteresis effects in ferroelectric ceramics. *International Journal of Solids and Structures* 2006; **43**:7197–7222.

[28] Smith RC. *Smart Material Systems: Model Development*, SIAM-Frontiers in Applied Mathematics, Philadelphia, 2005.

[29] Mayergoyz ID, Bertotti G. *The Science of Hysteresis*, vol. 3. Elsevier, 2005.

[30] Ge P, Jouaneh M. Generalized Preisach model for hysteresis nonlinearity of piezoceramic actuators. *Precision Engineering* 1997; **20**:99–111.

[31] Song G, Zhao J, Zhou X, De Abreu-Garcia JA. Tracking control of a piezoceramic actuator with hysteresis compensation using inverse Preisach model. *IEEE/ASME Transaction on Mechatronics* 2005; **10(2)**:198–209.

[32] Yu Y, Naganathan NG, Dukkipati RV. Preisach modeling of hysteresis for piezoceramic actuator systems. *Mechanism and Machine Theory* 2002; **37**:49–59.

[33] Zouari W, Zineb T, Benjeddou A. A FSDT-MITC Piezoelectric shell finite element with ferroelectric non-linearity. *Journal of Intelligent Material Systems and Structures* 2009; **20(17)**:2055-2075.

[34] Klinkel S, Gruttmann F, Wagner W. A mixed shell formulation accounting for thickness strains and finite strain 3d material models. *International Journal for Numerical Methods in Engineering* 2008; **75**:945–970.

[35] Lee HJ, Saravanos DA. The effect of temperature induced material property variations on piezoelectric composite plates. *AIAA* 1997; 1781–1788.

[36] Mauck LD, Lynch CS. Thermo-electro-mechanical behavior of ferroelectric material part I: A computational micromechanical model versus experimental results. *Journal of Intelligent Material Systems and Structures* 2003; **14**:587–602.

[37] Ren W, Liu SF, Mukherjee BK. Piezoelectric properties an phase transition of (001)-oriented Pb(Zn1/3Nb2/3)O3-PbTiO3 single crystals. *Applied Physics Letters* 2002; **80(17)**:3174–3176.

[38] Yimnirun R, Laosiritaworn Y, Wongsaenmai S, Ananta S. Scaling behavior of dynamic hysteresis in soft lead zirconate titanate bulk ceramics. *Applied Physics Letters* 2006; **89**:162901.

[39] Yimnirun R, Wongmaneerung R, Wongsaenmai S, Ngamjarurojana A, Ananta S, Laosiritaworn Y. Temperature scaling of dynamic hysteresis in soft lead zirconate titanate bulk ceramic. *Applied Physics Letters* 2007; **90**:112906.

[40] Smith RC, Hom CL. A temperature-dependent constitutive model for relaxor ferroelectrics. *Journal of Intelligent Material Systems and Structures* 2005; **16**:433–448.

[41] Yoshida K, Ikeda T, Ueda T. A constitutive model for temperature dependent behavior of ferroelectric materials. *Behavior and Mechanics of Multifunctional Materials and Composites, Proceedings of the SPIE Conf.* Ounaies Z, Li J (eds.) 2009; **7289**:72890J.

[42] Green AE, Naghdi PM. On the derivation of shell theories by direct approach *Journal of Applied Mechanics* 1974; **41**:173–176.

[43] Oh I. Thermopiezoelastic nonlinear dynamics of active piezolaminated plates *Smart Materials and Structures* 2005; **14**:823–834.

[44] Altenbach H, Altenbach J, Kissing W. *Mechanics of composite structural elements.* Springer, 1994.

[45] Preisach F. Über die magnetische Nachwirkung. *Zeitschrift für Physik* 1935; **94**:277–302.

[46] Sreeran P, Salvady G, Naganathan NG. Hysteresis prediction for a piezoceramic material system. *ASME Winter Annual Meeting (New Orleans, LA)* 1993; 35–42.

[47] Mayergoyz ID. *Mathematical Models of Hysteresis and Their Applications* (1st edn), vol. 1. Elsevier Series in Electromagnetism Elsevier, 2003.

[48] Barker JA, Schreiber DE, Huth BG, Everett DH. Magnetic hysteresis and minor loops: models and experiments. *Proceedings of the Royal Society of London. Series A,*. 1983; **386(1791)**251–261.

[49] Cardelli E, Della Torre E, Ban G. Experimental determination of preisach distribution functions in magnetic cores. *Physica B* 2000; **275**:262–269.

[50] Iyer RV, Shirley ME. Hysteresis parameter identification with limited experimental data. *IEEE Journal* 2004; **40(5)**:3227–3239.

[51] Butz A, Klinkel S, Wagner W. A geometrically and materially non-linear piezoelectric three-dimensional-beam finite element formulation including warping effects. *International Journal for Numerical Methods in Engineering* 2008; **76**:601–635.

[52] Taylor RL. Finite element analysis of linear shell problems. *The Mathematics of Finite Elements and Applications VI (MAFELAP 1987)* Whiteman JR (ed). Academic Press: London, 1988; 191–204.

[53] Dvorkin E, Bathe KJ. A continuum mechanics based four node shell element for general nonlinear analysis. *Engineering Computations* 1984; **1**:77–88.

[54] Simo JC, Rifai MS. A class of mixed assumed strain methods and the method of incompatible modes. *International Journal for Numerical Methods in Engineering* 1990; **29**:1595–1638.

[55] Gruttmann F, Wagner W. Structural analysis of composite laminates using a mixed hybrid shell element. *Computational Mechanics* 2006; **37(6)**:479–497.

[56] Simo JC, Fox DD, Rifai MS. On a stress resultant geometrically exact shell model. Part II: The linear theory; Computational aspects. *Computer Methods in Applied Mechanics and Engineering* 1989; **73**:53–92.

[57] Pian TTH, Sumihara K. Rational approach for assumed stress finite elements. *International Journal for Numerical Methods in Engineering* 1984; **20**:1685–1695.

[58] Tzou HS, Tsneg CI. Distributed vibration control and identification of coupled elastic/piezoelectric systems: Finite element formulation and application. *Mechanical Systems and Signal Processing* 1991; **5(3)**:215–231.

[59] Hwang WS, Park HC. Finite element modeling of piezoelectric sensors and actuators. *AIAA Journal* 1993; **31(5)**:930–937.

[60] Chee CYK, Tong L, Steven GP. A mixed model for composite beams with piezoelectric actuators and sensors. *Smart Materials and Structures* 1999; **8**:417–432.

[61] Tzou HS. Development of a light-weight robot end-effector using polymeric piezoelectric bimorph. *IEEE Conference on Robotics and Automation* 1989; 1704–1709.

[62] Sze KY, Pan YS. Hybrid finite element models for piezoelectric materials. *Journal of Sound and Vibration* 1999; **226**:519–547.

[63] Sze KY, Ghali A. Hybrid hexahedral element for solids, plates and beams by selective scaling. *International Journal of Numerical Methods in Engineering* 1993; **36**:1519–1540.

[64] Balamurugan V, Narayanan S. Shell finite element for smart piezoelectric composite plate-shell structures and its application to the study of active vibration control. *Finite Elements in Analysis and Design* 2001; **37(9)**:713–738.

[65] Saravanos DA. Mixed laminate theory and finite element smart piezoelectric composite shell structures. *AIAA Journal* 1997; **35(8)**:1327–1333.

[66] Gupta VK. *Studies on piezoelectric actuated shell with application to optimal steering of antenna* PhD Thesis. IIT Mumbai, India, 2003.

[67] Gupta VK, Seshu P, Kurien Issac K. Finite element and experimental investigation of piezoelectric actuated smart shells. *AIAA Journal* 2004; **42(10)**:2112–2123.

[68] Gupta VK, Seshu P, Kurien Issac K, Shevgaonkar RK. Optimal steering of paraboloid antenna using piezoelectric actuators. *Smart Materials and Structures* 2007; **16**:67–75.

[69] Alexander PW, Brei D, Miao W, Halloran JW, Gentilman RL, Schmidt GE, McGuire PT, Hollenbeck JR. Fabrication and experimental characterization of d_{31} telescopic piezoelectric actuators. *Journal of Materials Science* 2001; **36(17)**:4231–4237.

[70] Linnemann K, Klinkel S, Wagner W. A constitutive model for magnetostrictive and piezoelectric materials. *International Journal of Solids and Structures* 2009; **46(5)**:1149–1166.